The Astrophysical Journal, 1006:63 (17pp), 2026 July 20 https://doi.org/10.3847/1538-4357/ae801e

Gravitational-wave Measurement of the $M_{\rm BH}$–$M_{\rm bulge}$ Intrinsic Scatter at High Redshift

Cayenne Matt[1], Kayhan Gültekin[1], Gabriella Agazie[2], Nikita Agarwal[3,4], Akash Anumarlapudi[5], Anne M. Archibald[6], Zaven Arzoumanian[7], Jeremy G. Baier[8], Paul T. Baker[9], Bence Bécsy[10], Laura Blecha[11], Adam Brazier[12,13], Paul R. Brook[10], Sarah Burke-Spolaor[3,4,70], Rand Burnette[8], Robin Case[8], J. Andrew Casey-Clyde[14], Maria Charisi[15,16], Shami Chatterjee[12], Tyler Cohen[17], James M. Cordes[12], Neil J. Cornish[18], Fronefield Crawford[19], H. Thankful Cromartie[20,21], Kathryn Crowter[22], Megan E. DeCesar[21,23,71], Paul B. Demorest[24], Heling Deng[25], Lankeswar Dey[3,4], Timothy Dolch[26,27], Graham M. Doskoch[3,4], Elizabeth C. Ferrara[28,29,30], William Fiore[22], Emmanuel Fonseca[3,4], Gabriel E. Freedman[30], Emiko C. Gardiner[31], Nate Garver-Daniels[3,4], Peter A. Gentile[3,4], Kyle A. Gersbach[32], Joseph Glaser[3,4], Deborah C. Good[33], C. J. Harris[1], Jeffrey S. Hazboun[8], Ross J. Jennings[3,4,72], Aaron D. Johnson[2,34], Megan L. Jones[2], David L. Kaplan[2], Anala Kavumkandathil Sreekumar[3,4], Luke Zoltan Kelley[35], Matthew Kerr[36], Joey S. Key[37], Nima Laal[32], Michael T. Lam[38,39,40], William G. Lamb[32], Bjorn Larsen[41], T. Joseph W. Lazio[42], Natalia Lewandowska[43], Tingting Liu[44], Duncan R. Lorimer[3,4], Jing Luo[45,73], Ryan S. Lynch[46], Chung-Pei Ma[31,47], Dustin R. Madison[48], Ashley Martsen[3,4], Alexander McEwen[2], James W. McKee[49], Maura A. McLaughlin[3,4], Natasha McMann[32], Bradley W. Meyers[50,51], Patrick M. Meyers[52], Chiara M. F. Mingarelli[41], Andrea Mitridate[53], Cherry Ng[54], David J. Nice[55], Shania Nichols[38], Stella Koch Ocker[34,56], Ken D. Olum[57], Timothy T. Pennucci[58], Benetge B. P. Perera[59], Polina Petrov[32], Nihan S. Pol[60], Henri A. Radovan[61], Scott M. Ransom[62], Paul S. Ray[36], Joseph D. Romano[60], Jessie C. Runnoe[32], Alexander Saffer[62,72], Shashwat C. Sardesai[2], Ann Schmiedekamp[63], Carl Schmiedekamp[63], Kai Schmitz[64], Brent J. Shapiro-Albert[3,4,65], Xavier Siemens[2,8], Joseph Simon[66,74], Sophia V. Sosa Fiscella[39,40], Ingrid H. Stairs[22], Daniel R. Stinebring[67], Kevin Stovall[24], Abhimanyu Susobhanan[68], Joseph K. Swiggum[55,72], Jacob Taylor[8], Stephen R. Taylor[32], Mercedes S. Thompson[22], Jacob E. Turner[46], Michele Vallisneri[52], Rutger van Haasteren[68], Sarah J. Vigeland[2], Haley M. Wahl[3,4], Kevin P. Wilson[3,4], Caitlin A. Witt[69], David Wright[8], and Olivia Young[39,40]

[1] Department of Astronomy and Astrophysics, University of Michigan, Ann Arbor, MI 48109, USA; cayenne@umich.edu
[2] Center for Gravitation, Cosmology and Astrophysics, Department of Physics and Astronomy, University of Wisconsin-Milwaukee, P.O. Box 413, Milwaukee, WI 53201, USA
[3] Department of Physics and Astronomy, West Virginia University, P.O. Box 6315, Morgantown, WV 26506, USA
[4] Center for Gravitational Waves and Cosmology, West Virginia University, Chestnut Ridge Research Building, Morgantown, WV 26505, USA
[5] Department of Physics and Astronomy, University of North Carolina, Chapel Hill, NC 27599, USA
[6] Newcastle University, NE1 7RU, UK
[7] X-Ray Astrophysics Laboratory, NASA Goddard Space Flight Center, Code 662, Greenbelt, MD 20771, USA
[8] Department of Physics, Oregon State University, Corvallis, OR 97331, USA
[9] Department of Physics and Astronomy, Widener University, One University Place, Chester, PA 19013, USA
[10] Institute for Gravitational Wave Astronomy and School of Physics and Astronomy, University of Birmingham, Edgbaston, Birmingham, B15 2TT, UK
[11] Physics Department, University of Florida, Gainesville, FL 32611, USA
[12] Cornell Center for Astrophysics and Planetary Science and Department of Astronomy, Cornell University, Ithaca, NY 14853, USA
[13] Cornell Center for Advanced Computing, Cornell University, Ithaca, NY 14853, USA
[14] Department of Physics, University of Connecticut, 196 Auditorium Road, U-3046, Storrs, CT 06269-3046, USA
[15] Department of Physics and Astronomy, Washington State University, Pullman, WA 99163, USA
[16] Institute of Astrophysics, FORTH, GR-71110, Heraklion, Greece
[17] Department of Physics, New Mexico Institute of Mining and Technology, 801 Leroy Place, Socorro, NM 87801, USA
[18] Department of Physics, Montana State University, Bozeman, MT 59717, USA
[19] Department of Physics and Astronomy, Franklin & Marshall College, P.O. Box 3003, Lancaster, PA 17604, USA
[20] National Research Council Research Associate, National Academy of Sciences, Washington, DC 20001, USA
[21] Resident at Naval Research Laboratory, Washington, DC 20375, USA
[22] Department of Physics and Astronomy, University of British Columbia, 6224 Agricultural Road, Vancouver, BC V6T 1Z1, Canada
[23] Department of Physics and Astronomy, George Mason University, Fairfax, VA 22030, USA
[24] National Radio Astronomy Observatory, 1003 Lopezville Road, Socorro, NM 87801, USA
[25] Columbia Astrophysics Laboratory, Columbia University, 538 West 120th Street, New York, NY 10027, USA
[26] Department of Physics, Hillsdale College, 33 E. College Street, Hillsdale, MI 49242, USA
[27] Eureka Scientific, 2452 Delmer Street, Suite 100, Oakland, CA 94602-3017, USA
[28] Department of Astronomy, University of Maryland, College Park, MD 20742, USA
[29] Center for Research and Exploration in Space Science and Technology, NASA/GSFC, Greenbelt, MD 20771, USA
[30] NASA Goddard Space Flight Center, Greenbelt, MD 20771, USA
[31] Department of Astronomy, University of California, Berkeley, 501 Campbell Hall #3411, Berkeley, CA 94720, USA
[32] Department of Physics and Astronomy, Vanderbilt University, 2301 Vanderbilt Place, Nashville, TN 37235, USA
[33] Department of Physics and Astronomy, University of Montana, 32 Campus Drive, Missoula, MT 59812, USA
[34] Division of Physics, Mathematics, and Astronomy, California Institute of Technology, Pasadena, CA 91125, USA
[35] Astrophysics Working Group, NANOGrav Collaboration, Berkeley, CA 94720, USA
[36] Space Science Division, Naval Research Laboratory, Washington, DC 20375-5352, USA
[37] University of Washington Bothell, 18115, Campus Way NE, Bothell, WA 98011, USA
[38] SETI Institute, 339 N Bernardo Ave Suite 200, Mountain View, CA 94043, USA
[39] School of Physics and Astronomy, Rochester Institute of Technology, Rochester, NY 14623, USA
[40] Laboratory for Multiwavelength Astrophysics, Rochester Institute of Technology, Rochester, NY 14623, USA
[41] Department of Physics, Yale University, New Haven, CT 06511, USA

[42] Jet Propulsion Laboratory, California Institute of Technology, 4800 Oak Grove Drive, Pasadena, CA 91109, USA
[43] Department of Physics and Astronomy, State University of New York at Oswego, Oswego, NY 13126, USA
[44] Department of Physics and Astronomy, Georgia State University, 25 Park Place, Suite 605, Atlanta, GA 30303, USA
[45] Department of Astronomy & Astrophysics, University of Toronto, 50 Saint George Street, Toronto, ON M5S 3H4, Canada
[46] Green Bank Observatory, P.O. Box 2, Green Bank, WV 24944, USA
[47] Department of Physics, University of California, Berkeley, CA 94720, USA
[48] Department of Physics, Occidental College, 1600 Campus Road, Los Angeles, CA 90041, USA
[49] Department of Physics and Astronomy, Union College, Schenectady, NY 12308, USA
[50] Australian SKA Regional Centre (AusSRC), Curtin University, Bentley, WA 6102, Australia
[51] International Centre for Radio Astronomy Research (ICRAR), Curtin University, Bentley, WA 6102, Australia
[52] ETH Zurich, Institute for Particle Physics and Astrophysics, Wolfgang-Pauli-Strasse 27, 8093 Zurich, Switzerland
[53] Abdus Salam Centre for Theoretical Physics, Imperial College London, London SW7 2AZ, UK
[54] Dunlap Institute for Astronomy and Astrophysics, University of Toronto, 50 St. George Street, Toronto, ON M5S 3H4, Canada
[55] Department of Physics, Lafayette College, Easton, PA 18042, USA
[56] The Observatories of the Carnegie Institution for Science, Pasadena, CA 91101, USA
[57] Institute of Cosmology, Department of Physics and Astronomy, Tufts University, Medford, MA 02155, USA
[58] Institute of Physics and Astronomy, Eötvös Loránd University, Pázmány P. s. 1/A, 1117 Budapest, Hungary
[59] Arecibo Observatory, HC3 Box 53995, Arecibo, PR 00612, USA
[60] Department of Physics, Texas Tech University, Box 41051, Lubbock, TX 79409, USA
[61] Department of Physics, University of Puerto Rico, Mayagüez, PR 00681, USA
[62] National Radio Astronomy Observatory, 520 Edgemont Road, Charlottesville, VA 22903, USA
[63] Department of Physics, Penn State Abington, Abington, PA 19001, USA
[64] Institute for Theoretical Physics, University of Münster, 48149, Münster, Germany
[65] Giant Army, 915A 17th Avenue, Seattle WA 98122, USA
[66] Department of Astrophysical and Planetary Sciences, University of Colorado, Boulder, CO 80309, USA
[67] Department of Physics and Astronomy, Oberlin College, Oberlin, OH 44074, USA
[68] Max-Planck-Institut für Gravitationsphysik (Albert-Einstein-Institut), Leibniz Universität Hannover, Callinstraße 38, D-30167 Hannover, Germany
[69] Department of Physics, Wake Forest University, 1834 Wake Forest Road, Winston-Salem, NC 27109, USA

Received 2026 March 11; revised 2026 June 15; accepted 2026 June 18; published 2026 July 15

Abstract

The observed gravitational-wave background (GWB) spectrum is higher in amplitude than model predictions by a factor of 2–3. Using a semi-analytic model, we evaluate the effect of a high-scatter supermassive black hole (SMBH) scaling relation ($M_{\rm BH}$–$M_{\rm bulge}$) on models of the nanohertz GWB. By implementing an intrinsic scatter of the $M_{\rm BH}$–$M_{\rm bulge}$ relation, which is larger at higher redshift, but matches local observations, we find that the amplitude of GWB models increases to be consistent with the low-frequency end of the GWB spectrum. This amplitude increase is not uniform across frequencies, a strongly evolving scatter preferentially increases the number density of the most massive SMBHs which, in the GWB spectrum, minimizes the strength of the low-frequency turnover. Our models with positively evolving intrinsic scatter can reproduce the electromagnetically observed overmassive SMBHs at $4 < z < 6$ without changing the $M_{\rm BH}$–$M_{\rm bulge}$ normalization though we find that including moderate normalization evolution marginally improves fits to the GWB data. We conclude that the $M_{\rm BH}$–$M_{\rm bulge}$ relation which best describes the available GWB and electromagnetic data sets has intrinsic scatter that evolves as $\varepsilon(z) = \varepsilon_0 + (0.56 \pm 0.4)\log_{10}(1 + z)$ and normalization that evolves as $\alpha(z) = \alpha_0(1 + z)^{0.84\pm0.35}$. The results of this work imply that the $M_{\rm BH}$–$M_{\rm bulge}$ relation we see today is not universal throughout cosmic time and that a diversity of seeding models and growth mechanisms may be at play in the early stages of SMBH–galaxy evolution.

Unified Astronomy Thesaurus concepts: Black holes (162); Supermassive black holes (1663); Astrophysical black holes (98); Gravitational waves (678); Gravitational wave astronomy (675); Galaxies (573); Scaling relations (2031)

1. Introduction

Accurate models for the supermassive black hole (SMBH) mass function outside the local Universe are important, but poorly defined. Locally, we see a strong correlation between the SMBH mass and host galaxy bulge mass (J. Kormendy & L. C. Ho 2013; N. J. McConnell & C.-P. Ma 2013). Unfortunately, electromagnetic (EM)–based SMBH mass measurements become prohibitively difficult for more distant galaxies, meaning that correlations we observe locally, such as $M_{\rm BH}$–$M_{\rm bulge}$, are not well defined for higher redshifts. This relationship between SMBH and host bulge mass is a critical indicator of how galaxies and BHs evolve (together and/or separately). Where populations of SMBH–galaxy pairs lie on this relation through time provides insights into their rates of growth, feedback between growth mechanisms, and the relative importance and contributions of, e.g., accretion, star formation, and mergers for these objects.

Many studies have leveraged theory, EM observations, cosmological simulations, or gravitational waves to constrain the high-redshift location of this relation without general consensus (e.g., J. S. B. Wyithe & A. Loeb 2003; Y. Zhang

[70] Sloan Fellow.
[71] Resident at the Naval Research Laboratory.
[72] NANOGrav Physics Frontiers Center Postdoctoral Fellow.
[73] Deceased.
[74] NSF Astronomy and Astrophysics Postdoctoral Fellow.

et al. 2023; Y. Chen et al. 2024; F. Zou et al. 2024; C. Matt et al. 2026). A notable portion of these studies focus primarily on the normalization (y-intercept) of the $M_{\rm BH}$–$M_{\rm bulge}$ relation. Some EM-based studies find evidence for an increased $M_{\rm BH}$–$M_{\rm bulge}$ normalization in the past, which would imply a BH-first growth pathway, i.e., BH "dominance," where the BH growth initially outpaces that of the galaxy and/or BHs originate from heavy seeds (M. Volonteri 2012; M.-Y. Zhuang & L. C. Ho 2023). Other studies find no evidence for changes to the normalization with time (G. Mountrichas 2023; F. Zou et al. 2024; J. Li et al. 2025a; Y. Sun et al. 2025a; S. Geris et al. 2026). Since the launch of the James Webb Space Telescope (JWST) in 2021, numerous studies have reported SMBH and galaxy mass measurements at $z > 4$ (e.g., X. Ding et al. 2023; Y. Harikane et al. 2023; R. Maiolino et al. 2024; J. Li et al. 2025a), with no clear consensus on the intrinsic $M_{\rm BH}$–$M_{\rm bulge}$. It is possible that the discrepancy between results could arise due to observational biases in some magnitude-limited surveys, which would leave lower-mass SMBHs unobserved and thus artificially inflate the amplitude and flatten the relation (T. R. Lauer et al. 2007; H. Zhang et al. 2023; J. Li et al. 2025b). It has been suggested that there are lower-mass SMBHs at high redshift that evade detection (F. Shankar et al. 2016, 2019; J. D. Silverman et al. 2025; F. Ziparo et al. 2026).

Recently, J. Li et al. (2025a) selected active galactic nuclei (AGNs) from archival JWST data based on the presence of a broad Hα component rather than using a magnitude/luminosity cutoff. The result of this selection was a population of SMBH–galaxy pairs with mass ratios consistent with the local AGN relations. This result suggests that many surveys that find exclusively overmassive SMBHs may be incomplete and the offset of the $M_{\rm BH}$–$M_{\rm bulge}$ relation at $z > 4$ relative to today is less extreme (and possibly zero). If this is the case, then perhaps the normalization is not higher; however, the local relation still does not predict these extremely high-mass SMBHs seen at $z > 4$. An alternative explanation is that the intrinsic scatter of the $M_{\rm BH}$–$M_{\rm bulge}$ relation was higher in the past, therefore reproducing these overmassive BHs without needing extreme SMBH growth on a population level. This hypothesis simultaneously predicts a large population of normal and low-mass-ratio SMBH–galaxy pairs (J. Li et al. 2025a; M. Brooks et al. 2026; S. Geris et al. 2026).

Locally, the $M_{\rm BH}$–$M_{\rm bulge}$ relationship has relatively low intrinsic scatter (second only to the $M_{\rm BH}$–σ relation; L. Ferrarese & D. Merritt 2000; K. Gebhardt et al. 2000; S. Tremaine et al. 2002; K. Gültekin et al. 2009, 2011; J. Kormendy & L. C. Ho 2013; N. J. McConnell & C.-P. Ma 2013; J. E. Greene et al. 2016). This correlation implies a coupled growth pathway for SMBH–galaxy pairs, and the scatter about this relationship reflects small differences in growth rates (M.-Y. Zhuang & L. C. Ho 2023; B. A. Terrazas et al. 2025; D. Izquierdo-Villalba 2026) and, at the low-mass end, seed information (J. E. Greene et al. 2020; T. K. Waters et al. 2026, in preparation). If the growth rates of both galaxies and their central SMBHs were to be roughly similar, then objects would grow along the $M_{\rm BH}$–$M_{\rm bulge}$ relation with cosmic time. Galaxy–SMBH pairs would be born in the low-mass region of the relation and evolve up, following the slope of the relation until they reach their present-day masses. In this case, the $M_{\rm BH}$–$M_{\rm bulge}$ relation would be a valuable tool for predicting SMBH masses based on galaxy bulge masses for distant galaxies where the SMBH is obscured and/or the spectral resolution is too low to make direct SMBH mass measurements. Indeed, some studies have found that both the normalization and scatter of the $M_{\rm BH}$–$M_{\rm bulge}$ relation are unchanging with time (C. A. Guia & F. Pacucci 2024; F. Zou et al. 2024), although these results fail to predict the massive SMBHs at $z > 4$.

An increased intrinsic scatter could indicate that there is a diversity of growth pathways for SMBHs and galaxies (M.-Y. Zhuang & L. C. Ho 2023; H. Hu et al. 2025; B. A. Terrazas et al. 2025; D. Izquierdo-Villalba 2026). For example, overmassive SMBH hosts have high star formation rates so the galaxy can catch up in mass. Conversely, undermassive SMBHs have low star formation rates and high Eddington ratios (and high AGN luminosities) because they are growing their SMBHs to catch up. Then, pairs can stay on the relation when they have positive star formation/accretion feedback and merger-based growth. Independently, an increased scatter in the past but a low scatter locally is predicted even if there is no physical link between SMBH and host galaxy mass (K. Jahnke & A. V. Macciò 2011). Furthermore, M. Hirschmann et al. (2010) modeled the change in scatter because of mergers and found that the scatter decreases with the number of mergers because of central limit theorem considerations. More recently, B. Zhu & V. Springel (2025) compared the sources of intrinsic scatter through time in various cosmological simulations. Their results showed that the dominant source and scale of scatter of the $M_{\rm BH}$–$M_{\rm bulge}$ relation can change both with redshift and mass, indicating that the value of scatter outside the local Universe can provide important insights into SMBH–galaxy coevolution. Other studies have found that some cosmological simulations can reproduce the overmassive population of SMBHs seen by JWST with large values of intrinsic scatter (S. Dattathri et al. 2025).

EM-based constraints on the $M_{\rm BH}$–$M_{\rm bulge}$ relation remain difficult. There are two major limitations that lead to the underdetection of low $M_{\rm BH}/M_\star$ ratios: (i) low-luminosity AGNs in massive galaxies are difficult to see because they are outshined by the host (e.g., M. Volonteri et al. 2023; J. Li et al. 2025b; J. D. Silverman et al. 2025); and (ii) low-luminosity AGNs are difficult/impossible to find in magnitude-limited surveys (e.g., T. R. Lauer et al. 2007; A. Schulze & L. Wisotzki 2014; J. Li et al. 2025b). Gravitational waves produced by SMBH binaries do not face these same challenges. It has long been theorized that we can get constraints from the nanohertz gravitational-wave background (GWB; J. Simon & S. Burke-Spolaor 2016). There is now strong evidence of a detection of the GWB from pulsar timing arrays (PTAs; G. Agazie et al. 2023a; EPTA Collaboration et al. 2023; D. J. Reardon et al. 2023; H. Xu et al. 2023). Since the 4σ evidence announcement, there has been a surge of analyses placing constraints on SMBH populations (G. Agazie et al. 2023b; Y. Chen et al. 2024; E. C. Gardiner et al. 2024; E. R. Liepold & C.-P. Ma 2024; G. Sato-Polito et al. 2024; S. Bonoli et al. 2025; C. Matt et al. 2026). Though the details vary between these studies, the broad consensus is that the unexpectedly high GWB amplitude requires more high-mass SMBHs than predicted by the local $M_{\rm BH}$–$M_{\rm bulge}$ relation. Some studies have focused on the SMBH–galaxy relations themselves, while others have revised our predictions for galaxy populations (E. R. Liepold & C.-P. Ma 2024; G. Sato-Polito et al. 2024; C. Matt et al. 2026). There is now strong evidence to suggest that there are high-redshift SMBH–galaxy pairs that lie both above and on the local relation, leading to conflicting narratives of how the $M_{\rm BH}$–$M_{\rm bulge}$ relation may evolve (F. Pacucci et al. 2023; J. Li et al. 2025a). An $M_{\rm BH}$–$M_{\rm bulge}$ relation with an intrinsic scatter that was higher at earlier epochs increases the number of high- and low-mass SMBHs relative to the local relation for $z > 0$. This boost in high-mass SMBHs can amplify the predicted amplitude of the GWB and produce a population of overmassive SMBHs at high redshift while maintaining the same fundamental SMBH–galaxy mass relationship observed locally.

In this work, we consider a model for the GWB that uses an $M_{\rm BH}$–$M_{\rm bulge}$ relation with an evolving intrinsic scatter. We evaluate the potential of this model to unify EM and gravitational-wave observations across a wide range of redshifts.

In Section 2, we describe our model setup and the functional form of the scaling relations and parameter evolution. We describe the behavior of and effect of evolutionary parameters on our models in Section 3. The GWB-based results of our model fits are presented in Section 4, while comparisons with EM data are presented in Section 5. We place our findings into context in Section 7, and a summary of this work can be found in Section 8.

We assume WMAP9 cosmology (Planck Collaboration et al. 2014), and all values and parameters reported in log space are base 10 unless otherwise specified.

2. Semianalytic Models

We use a semianalytic SMBH binary population synthesis code, HOLODECK, to calculate the expected GWB spectrum. We briefly describe the model setup here, though a description of the model workflow and, e.g., SMBH binary hardening models can be found in G. Agazie et al. (2023b), with updates and recent changes further detailed in L. Z. Kelley et al. (2024) and C. Matt et al. (2026).

We assume an initial distribution of the SMBH total mass ($M_{\rm tot}$), mass ratio ($q = m_1/m_2$), and redshift, from which we define a population of merging galaxies based on the merger-rate prescription in V. Rodriguez-Gomez et al. (2015) and the galaxy stellar mass function (GSMF) in J. Leja et al. (2020). We then convert this distribution of galaxies into a population of SMBH binaries by assuming binaries are formed following a galaxy merger. Their masses are assigned based on the galaxy bulge masses via the $M_{\rm BH}$–$M_{\rm bulge}$ relation. This gives the number density of SMBH binaries per unit mass, mass ratio, and redshift, which are then evolved from $\sim$10 kpc separations down to the gravitational-wave regime according to the binary hardening prescription in L. Z. Kelley et al. (2017) and G. Agazie et al. (2023a). The non-gravitational-wave binary hardening processes include dynamical friction and stellar scattering, and we allow for hardening timescales long enough that some binaries effectively stall and not every galaxy merger results in an SMBH binary that contributes to the GWB. The GWB amplitude is then calculated following E. S. Phinney (2001).

Locally, the relationship between the SMBH mass and galaxy bulge mass follows a power-law relation (see, e.g., J. Kormendy & K. Gebhardt 2001; J. Kormendy & L. C. Ho 2013; N. J. McConnell & C.-P. Ma 2013). In our model, we define the $M_{\rm BH}$–$M_{\rm bulge}$ relation to be

$$M_{\rm BH} = \alpha_0\left(\frac{M_{\rm bulge}}{10^{11}\quad M_\odot}\right)^{\beta_0}, \tag{1}$$

with an intrinsic scatter in $\log M_{\rm BH}$ drawn from a normal distribution (K. Gültekin et al. 2009) with standard deviation ε_0. In this paper, we consider a scatter that is a function of redshift given by the form

$$\varepsilon(z) = \varepsilon_0 + \varepsilon_z \log(1 + z), \tag{2}$$

where the $z = 0$ values can be determined from observation ($\log \alpha_0 = 8.69$; $\beta_0 = 1.17$; $\varepsilon_0 = 0.28$ dex; J. Kormendy & L. C. Ho 2013), and ε_z can be positive or negative, with $\varepsilon_z = 0$ indicating no evolution in the relation. The intrinsic scatter in the relation is the scatter in the SMBH masses; it is explicitly incorporated into the $M_{\rm BH}$–$M_{\rm bulge}$ relation in HOLODECK and was a free parameter in both G. Agazie et al. (2023b) and C. Matt et al. (2026), though it was assumed to be unchanging with redshift. It has been suggested that the scatter in the $M_{\rm BH}$–$M_{\rm bulge}$ relation may be different for high- versus low-mass SMBHs (J. E. Greene et al. 2020). The available data from the GWB cannot currently constrain SMBH masses at $M_{\rm BH} \lesssim 10^8\, M_\odot$ (G. Agazie et al. 2023b). Therefore, we are only interested in the most massive SMBHs and a mass-independent intrinsic scatter is sufficient for our analysis.

For this work, we consider three models: two with a variable scatter evolution power law, ε_z, and one where ε_z is fixed to 0.5. A summary of the model setups can be found in Table 1. Our prior on ε_z is uniform, with $-0.2 \leqslant \varepsilon_z \leqslant 2.0$, as the ε_z parameter is only physically meaningful inside this range. If $\varepsilon_z < -0.2$, the intrinsic scatter drops below $\varepsilon_z \sim 0.1$ by $z \sim 2$. With $\varepsilon_z > 2.0$, SMBHs get scattered outside the nanohertz gravitational-wave regime, and roughly 30%–40% of galaxies with $M_\star > 10^{10}\, M_\odot$ have an SMBH–galaxy bulge mass ratio above 1 by $z \sim 3$. There is sufficient evidence from EM observations to rule out a high-redshift $M_{\rm BH}$–$M_{\rm bulge}$ relation with lower intrinsic scatter than the local value of 0.28 dex, but we still allow our lower range to include some negative evolution for model freedom and so we can be sure that the result is purely driven by our data.

In model $M_{\varepsilon+}$, we chose to sample three hardening parameters: the total hardening time, τ_f; the stellar scattering power-law slope, $\nu_{\rm inner}$; and the characteristic hardening radius, $R_{\rm char}$. These parameters can have strong impacts on the shape of the GWB spectrum (B. Kocsis & A. Sesana 2011; A. Sesana 2013; G. Agazie et al. 2023b; N. Laal et al. 2026). As discussed in the following section, the $M_{\rm BH}$–$M_{\rm bulge}$ scatter evolution also has an impact on the GWB spectral shape. We therefore allow these hardening parameters to vary for one model to investigate any possible degeneracies. We additionally sample three GSMF parameters: the two local normalizations, $\phi_{*,0,0}$ and $\phi_{*,1,0}$, and the local characteristic mass, $M_{\rm c,0}$. Previous GWB studies have found degeneracies between the GSMF and $M_{\rm BH}$–$M_{\rm bulge}$ parameters (G. Agazie et al. 2023b; C. Matt et al. 2026). To address these degeneracies, we fix them for model M_ε and model M_α, but we leave them variable in model $M_{\varepsilon+}$, to investigate how this affects our results.

To determine our best-fit models and posteriors, we draw 20,000 samples directly from our prior space, using Latin

Table 1
A Summary of the Parameter Setup for the Three Models in This Paper

Parameter	Purpose	Model M_{ε}	Model $M_{\varepsilon+}$	Model M_{α}
		$M_{\rm BH}$–$M_{\rm bulge}$		
ε_z	Scatter evolution	$\mathcal{U}[-0.2, 2.0]$	$\mathcal{U}[-0.2, 2.0]$	0.5
α_z	Normalization evolution	0.0	0.0	$\mathcal{U}[-3.0, 3.0]$
$\log \alpha_0$	Local normalization	8.69	$\mathcal{N}[8.69, 0.05]$	8.69
β_0	Local slope	1.17	$\mathcal{N}[1.17, 0.08]$	1.17
		SMBH Binary Hardening		
τ_f (Gyr)	Total binary lifetime	3.0	$\mathcal{U}[0.1, 11.0]$	3.0
$\nu_{\rm inner}$	Stellar scattering exponent	−1.0	$\mathcal{U}[-2.0, 0.0]$	−1.0
$R_{\rm char}$ (pc)[a]	Characteristic radius	10.0	$\mathcal{U}[2.0, 20.0]$	10.0
		GSMF		
$\phi_{*,0,0}$	Local normalization of first Schechter	−2.383	$\mathcal{N}[-2.383, 0.28]$	−2.383
$\phi_{*,1,0}$	Local normalization of second Schechter	−2.818	$\mathcal{N}[-2.818, 0.050]$	−2.818
$M_{c,0}$	Local characteristic mass	10.767	$\mathcal{N}[10.767, 0.026]$	10.767

Note. We note fixed parameters by single values and free parameters by their prior distributions. Both model M_{ε} and model M_{α} have one free parameter, while model $M_{\varepsilon+}$ allows nine parameters to vary. We use uniform distributions for the $M_{\rm BH}$–$M_{\rm bulge}$ evolutionary parameters (ε_z and α_z) and SMBH binary hardening parameters. We use the same priors for τ_f and $\nu_{\rm inner}$ as in G. Agazie et al. (2023b). For the local $M_{\rm BH}$–$M_{\rm bulge}$ and GSMF parameters, we use Gaussian priors based on J. Kormendy & L. C. Ho (2013) and J. Leja et al. (2020). All additional parameters not in this table are fixed to their fiducial value (C. Matt et al. 2026) for all three models.

[a] G. Agazie et al. (2023b) assumed a fixed value of $R_{\rm char} = 100$ pc. In the absence of other changes, our lower value increases the strength of the low-frequency turnover of the GWB spectrum.

hypercube sampling, and calculate the GWB spectrum for each sample instance using HOLODECK. We determine the goodness of fit by comparing each of the 20,000 spectra to the data and calculating a likelihood. The spectrum with the highest likelihood is our best-fit model. The likelihoods we calculate represent how well models fit the GWB data, but are not marginalized over the priors. Our posteriors are then the priors weighted by the likelihoods. This method was used by C. Matt et al. (2026) and was first described in the appendix of G. Agazie et al. (2023b).

3. Impact of Evolutionary Parameters

To aid in the interpretation of the results, we describe the isolated impact of two types of $M_{\rm BH}$–$M_{\rm bulge}$ evolution on the GWB spectrum and BH mass function (BHMF) in this section. The GWB amplitude is sensitive to the number of most massive SMBHs (E. S. Phinney 2001), so changes to the $M_{\rm BH}$–$M_{\rm bulge}$ relation that can increase the number of massive SMBHs will increase the predicted GWB amplitude in the absence of any other change. Both an increased $M_{\rm BH}$–$M_{\rm bulge}$ scatter and normalization will produce a greater number of massive SMBHs and so we would expect that either change could increase the predicted GWB amplitude.

Intuitively, one might initially expect the impact of increasing scatter to be similar to increasing normalization, although we find the effects to be more complex. In Figure 1, we compare the effect of an evolving scatter (top row) with that of an evolving $M_{\rm BH}$–$M_{\rm bulge}$ normalization (bottom row). In the left-hand column, we show the $z = 2$ BHMF, as calculated using different values of ε_z and α_z, indicating different strengths of evolution in scatter and normalization. Here, α_z is the normalization analog of ε_z ($\alpha(z) = \alpha_0(1 + z)^{\alpha_z}$; i.e., the same evolutionary form as C. Matt et al. 2026). The black/darkest blue line in every panel is the model with no redshift evolution of the $M_{\rm BH}$–$M_{\rm bulge}$ relation. The lighter colors correspond to greater values of the corresponding evolutionary parameter and therefore represent $M_{\rm BH}$–$M_{\rm bulge}$ relations with greater scatter/normalization at $z = 2$ than observed locally. We note that our fiducial (nonevolving) BHMF overpredicts the SMBH number density compared to AGN-inferred BHMFs—a discrepancy discussed in some detail by, e.g., E. R. Liepold & C.-P. Ma (2024).

In the left-hand column of Figure 1, we see that both types of positive evolution increase the number density of the most massive SMBHs, and the amount of the increase is correlated with the strength of the evolution. An increased $M_{\rm BH}$–$M_{\rm bulge}$ normalization is equivalent to increasing every calculated SMBH mass by some amount. The effect of increasing the SMBH mass is to shift the entire BHMF to the right on the x-axis (lower-left panel). The horizontal difference between any two curves is roughly equivalent across the entire mass range, but the vertical difference (number density) is greater at high masses, because of the steeper slope relative to the low-mass end. Increasing the intrinsic scatter shifts the SMBH masses both higher and lower, so the relative shift along the x-axis is identical across the mass range. In fact, the greatest increase is to the highest-mass number densities, and there are only negligible changes to the low-mass number densities. Though more commonly discussed in the context of observational bias, this effect is the same as that causing Eddington bias (A. S. Eddington 1913).

These parameters have differing effects at high and low masses, which affects not only the predicted BHMF, but also the associated GWB spectrum. In the right-hand column of Figure 1, we show the GWB spectrum associated with the same values for evolutionary parameters as in the left-hand panel. The color coding is the same across the columns. The GWB spectra are calculated with HOLODECK across $0 \leqslant z \leqslant 10$. For an equal-mass circular binary, the frequency of the gravitational waves emitted is twice the orbital

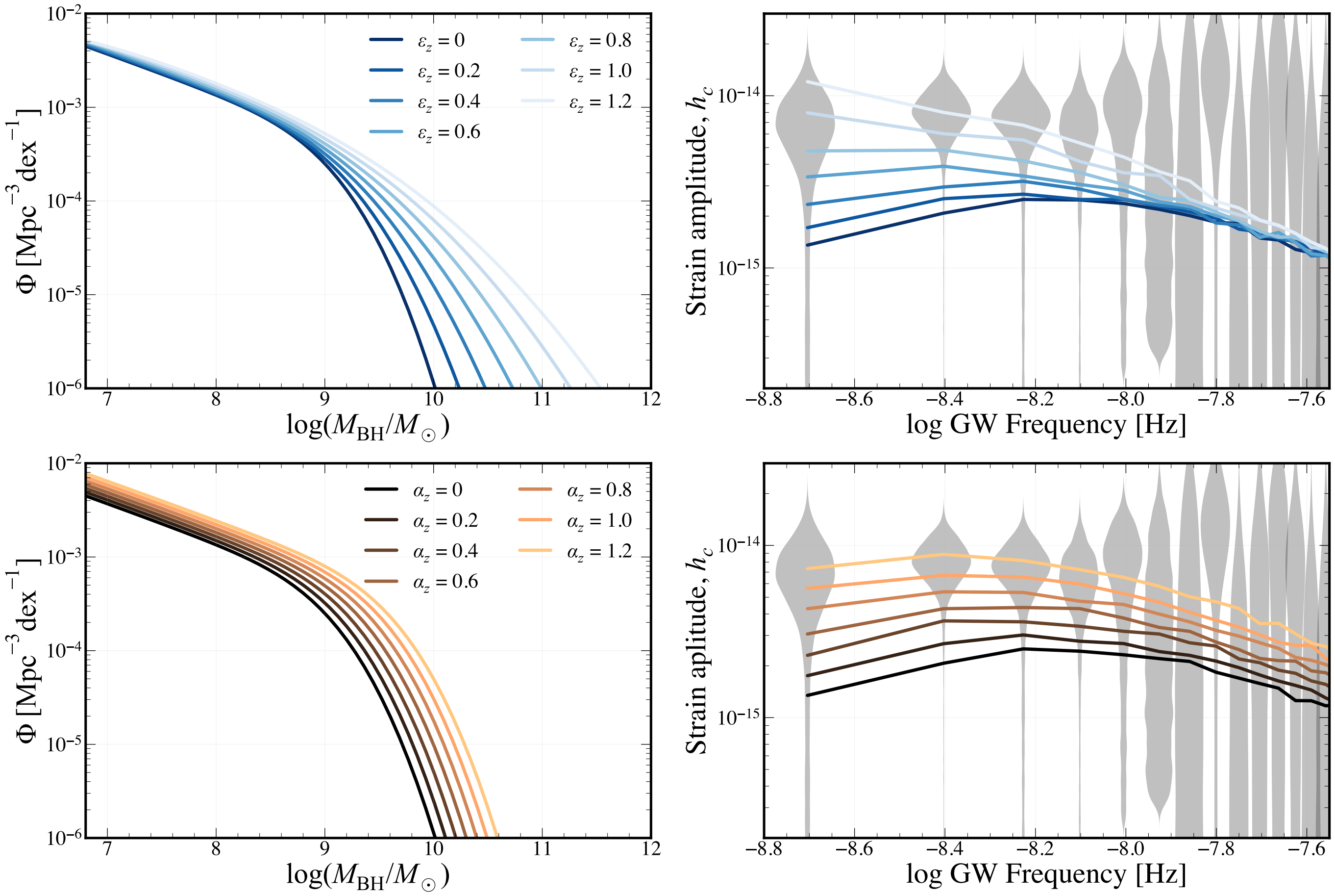

Figure 1. Here, we show the separate effects of an evolving $M_{\rm BH}$–$M_{\rm bulge}$ scatter (top) and normalization (bottom) on the $z = 2$ BHMF (left) and the GWB spectrum (right). We keep all parameters in the models constant and change only the power law for evolving scatter, ε_z (or that for evolving normalization, α_z), where ε_z, $\alpha_z = 0$ indicates no redshift evolution and ε_z, $\alpha_z > 0$ indicates positive redshift evolution. Both types of evolution increase the number density of the most massive SMBHs, where the amount of the increase is correlated with the strength of the evolution, but only an evolving normalization significantly increases the number density of SMBH masses $M_{\rm BH} < 10^9\,M_\odot$. The gravitational-wave frequency is inversely proportional to SMBH chirp mass. Therefore, the relative changes to number densities across the mass range have corresponding impacts on the GWB spectrum. Both types of evolution increase the amplitude at the lowest frequencies (highest masses), but only α_z affects the high-frequency (low-mass) end of the spectrum.

frequency. The orbital frequency of the binary is related to the masses of the SMBHs via Kepler's third law, so the lower frequencies of the GWB correspond to higher SMBH chirp masses ($f_{\rm GW,obs} \propto (M(1+z))^{-1}$; see E. S. Phinney 2001). Therefore, the relative changes to the number densities across the mass range have corresponding impacts on the GWB spectrum. Both types of evolution increase the GWB amplitude at the lowest frequencies (highest masses), but only α_z affects the high-frequency (low-mass) end of the spectrum. The difference in GWB amplitudes is strongest for $\log f_{\rm GW} \gtrsim -8.0$, where the the GWB data are poorly constrained, but there are still notable differences across the range we fit to (the five lowest-frequency bins).

The GWB spectrum produced by a population of SMBH binaries that harden only via gravitational-wave emission is a power law (E. S. Phinney 2001). Deviations from this power law can occur for a variety of reasons, but a turnover at the low-frequency end is expected if additional hardening mechanisms are present (B. Kocsis & A. Sesana 2011; A. Sesana 2013). Previous studies have found that the GWB data are well described by a spectrum with a turnover due to environmental effects (G. Agazie et al. 2023b; C. J. Harris et al. 2026). The underlying model we use to produce this figure includes both stellar scattering and dynamical friction as hardening mechanisms prior to the gravitational-wave emission phase. The turnover is apparent in the black (fiducial) spectrum from the curved shape (i.e., it is not a straight-line power law). Furthermore, we choose a characteristic hardening radius that is lower than in G. Agazie et al. (2023b), which serves to increase the strength of the turnover in this fiducial model. This turnover is unaffected by changes to the $M_{\rm BH}$–$M_{\rm bulge}$ normalization, but a strongly evolving scatter straightens the spectrum out, apparently approaching a power law. This shape change in the evolving scatter model is due to the frequency-dependent increase in GWB amplitude that is a result of the preferential increase in number density of the most massive SMBHs. The impact that a high $M_{\rm BH}$–$M_{\rm bulge}$ intrinsic scatter has on the spectrum seems to have a similar but opposite effect to the presence of environmental hardening. This makes disentangling the contributions from each of these population parameters difficult. Since the GWB data do show a turnover, this could mean that either the $M_{\rm BH}$–$M_{\rm bulge}$ scatter cannot evolve strongly or that environmental effects may be more important for recovering the spectral shape.

These differences, though large, require high-confidence data and precise population statistics to differentiate. Separating these effects is most feasible when only one type of evolution is present and the strength of evolution is great. If

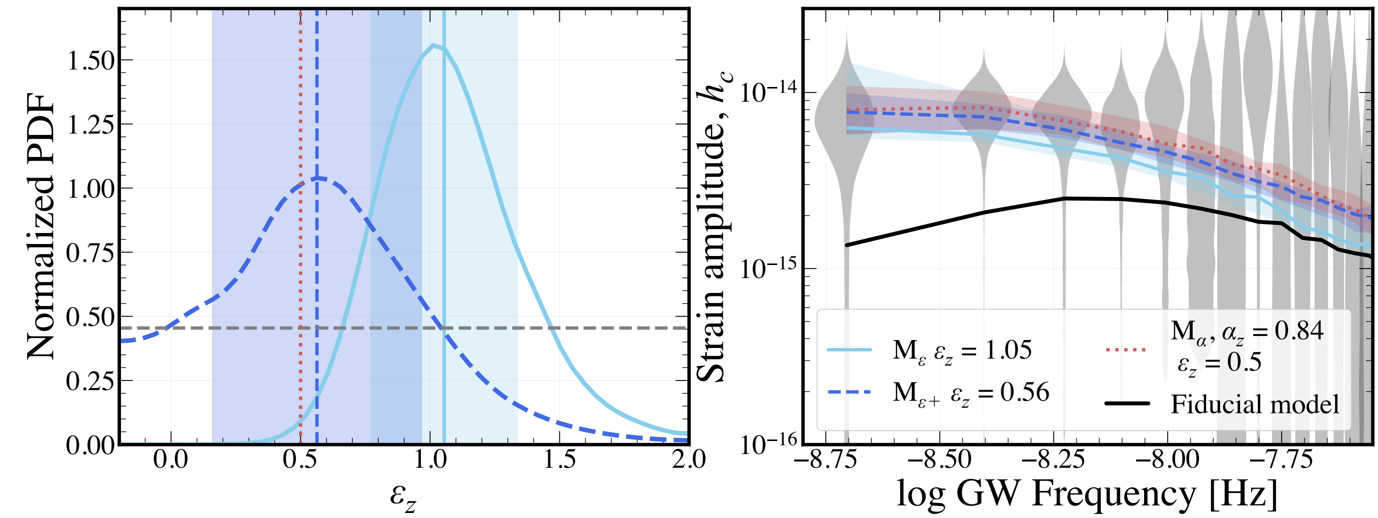

Figure 2. Left: the posterior distributions for ε_z from model M_ε (light blue solid line) and model $M_{\varepsilon+}$ (dark blue dashed line). The vertical lines represent the median of the posteriors; for model M_α (red dotted line), ε_z was fixed to a value of 0.5, so there is no distribution associated with the median line. The median value of model M_ε is higher than that of model $M_{\varepsilon+}$ because it had no additional free parameters to increase the amplitude and so ε_z had to compensate more. Right: the best-fit GWB spectra associated with our three models (blues and red) and the fiducial model (black). We see that all best-fit models have similar amplitudes and shapes. Both model $M_{\varepsilon+}$ and model M_α lie within the 68% confidence regions of the data, except for the fifth frequency bin, whereas model M_ε lies just below the 68% confidence regions of all but the lowest-frequency bin. All best-fit models are within the 95% confidence regions for the five frequency bins we fit to. The low-frequency turnover is present in all three best-fit models, though it is not strong. Notably, model M_ε lies below the other two models, and the bulk of the data only truly align with the lowest-frequency bin. Interestingly, the spectra of model $M_{\varepsilon+}$ and model M_α are quite similar, despite model $M_{\varepsilon+}$ having no evolution in the M_{BH}–M_{bulge} normalization.

either one is subtle (low values of α_z and/or ε_z) or if both types of evolution are present, the problem becomes difficult to disentangle. We compare between models that allow for multiple evolutionary paths of M_{BH}–M_{bulge} and place constraints using both EM and GWB data in Section 5.

4. Results

We show the results of all our models in Figure 2. The black line with the strong turnover is our fiducial model. This model was not sampled; this is simply the GWB spectrum that we would expect when using the default values for every parameter and no evolution in the M_{BH}–M_{bulge} relation (i.e., the same as the $\varepsilon_z = 0$ and $\alpha_z = 0$ spectra in the right-hand column of Figure 1). We do not perform fits to the data with a nonevolving M_{BH}–M_{bulge}; we instead point readers to C. Matt et al. (2026), who use the same fiducial model and did perform nonevolving M_{BH}–M_{bulge} fits. To compare the different models' ability to reproduce the GWB data, we perform likelihood ratio tests using the likelihoods we calculate during the fitting process for each spectrum. These are presented at the end of Section 4.3.

4.1. Model M_ε: The Isolated Effect of ε_z

Our first model, model M_ε, had ε_z as the only free parameter. Every other variable in the models is fixed to its fiducial value. This model isolates the effects of ε_z on the GWB spectrum. In the top row of Figure 1, we keep all parameters fixed, while varying only ε_z. This is the exact setup for model M_ε, except with a significantly decreased number of samples of ε_z.

The posterior distribution of ε_z in model M_ε (light blue solid line) is apparently Gaussian and centered on $\varepsilon_z = 1.05 \pm 0.28$, indicating a strong positive evolution of the M_{BH}–M_{bulge} scatter. The amplitude of the spectrum falls just short of the 68% confidence region of the observed GWB, except in the lowest-frequency bin. With only one parameter to vary, this

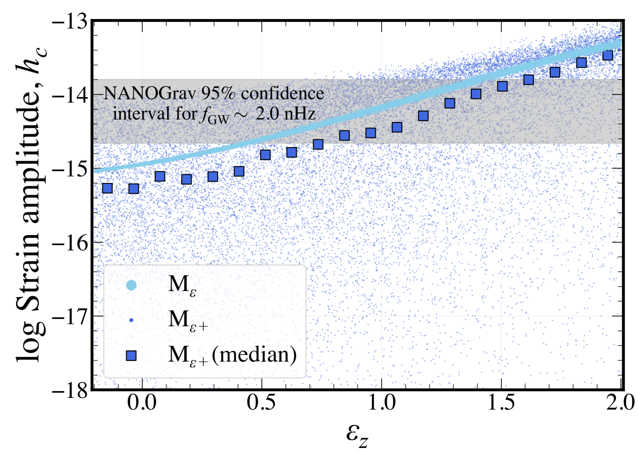

Figure 3. In this figure, we plot the log strain GWB amplitude, h_c, measured at the lowest-frequency bin $f_{\mathrm{gw}} \sim 2$ nHz against samples of ε_z drawn from our prior distribution. We show how the GWB amplitude of a model correlates with the sampled value of ε_z for model M_ε and model $M_{\varepsilon+}$. The dark blue points with large spread are from model $M_{\varepsilon+}$, where the blue squares represent the corresponding median log strain amplitude binned along the x-axis. The light blue line is from model M_ε, which has ε_z as the only free parameter. On average, there is a clear positive correlation between the GWB amplitude and the value of ε_z. We allow many parameters to vary in model $M_{\varepsilon+}$, and so the correlation between the GWB amplitude and ε_z is less direct. It is still present (blue squares), but there is a larger spread. Other parameters in the model have a strong correlation with the GWB amplitude (e.g., the local M_{BH}–M_{bulge} normalization, α_0), so the model does not need to rely solely on ε_z to reproduce the GWB amplitude. This indirect correlation causes the posterior distribution of ε_z to spread out, relative to smaller models. Values of ε_z that do not provide good fits to the GWB data in model M_ε can result in a well-fitting spectrum with model $M_{\varepsilon+}$ because of the effects of other parameters.

result makes sense; the fiducial spectrum is low in amplitude, and the value of ε_z correlates positively with the GWB amplitude (see Figure 3), therefore positive evolution of the M_{BH}–M_{bulge} scatter is favored. Since ε_z has less of an effect on higher frequencies, the ability for this single-parameter model to match all five of the lowest-frequency bins is limited, and the spectrum will systematically underpredict the data with increasing discrepancy as the frequency increases (assuming agreement in the lowest-frequency bin).

This spectrum is the worst fit to the data out of our three models (see Section 4.3). It is, however, significantly improved over the fiducial model, and so while evolving the scatter is not a complete solution, it appears to bridge the majority of the gap between the simplest models and observations. In the following sections, we describe how other parameters can resolve the remaining discrepancy.

4.2. Model $\mathrm{M}_{\varepsilon+}$: Effect of ε_z in the Presence of Additional Degrees of Freedom

Model $M_{\varepsilon+}$ sampled nine total parameters: ε_z, three hardening parameters (τ_f, ν_{inner}, and R_{char}), the local normalization and slope of the M_{BH}–M_{bulge} relation (α_0 and β_0), and the three local GSMF parameters ($\phi_{*,0,0}$, $\phi_{*,1,0}$, and $M_{\mathrm{c},0}$). For the M_{BH}–M_{bulge} relation and GSMF parameters, we use informative priors based on EM observations (J. Kormendy & L. C. Ho 2013; J. Leja et al. 2020), while we use uniform priors for the hardening parameters (L. Z. Kelley et al. 2017; G. Agazie et al. 2023b).

In Figure 2, the posterior distribution of ε_z for model $M_{\varepsilon+}$ (dark blue dashed line) favors lower values than with model M_{ε}, but 92% of the distribution corresponds to positive values of ε_z, with a median of $\varepsilon_z = 0.56 \pm 0.40$. Despite the more modest scatter evolution, the spectrum associated with this model is higher in amplitude than that of model M_{ε} and is in better agreement with the data, sitting within the 68% confidence region for the four lowest-frequency bins. All GSMF and local M_{BH}–M_{bulge} posteriors are in good agreement with the priors. C. Matt et al. (2026) found that for a nonevolving M_{BH}–M_{bulge} relation, the posterior distributions for these parameters will deviate significantly from the priors. Since these parameters are well constrained with EM observations (J. Kormendy & L. C. Ho 2013; J. Leja et al. 2020), congruency between posteriors and priors here indicates consistency with EM-based observations. With a weaker M_{BH}–M_{bulge} scatter evolution (versus model M_{ε}), we would expect the amplitude of the GWB to be lower. However, the correlation between ε_z and GWB amplitude is less direct with so many additional free parameters.

In Figure 3, we show a scatter plot of the GWB amplitude versus ε_z. As described in Section 2, for each of the 20,000 samples taken from our prior distributions, we calculate a GWB spectrum. In Figure 3, we plot the amplitude of those 20,000 spectra (at the lowest-frequency bin, $\log f_{\mathrm{GW}} \sim -8.7$) for both model M_{ε} and model $M_{\varepsilon+}$ versus the value of ε_z for the associated sample.

The light blue line corresponds to model M_{ε}, which sampled only ε_z, and the dark blue points are from model $M_{\varepsilon+}$, which sampled nine total parameters. The blue squares represent the median of the dark blue points, binned along ε_z. For model M_{ε}, the GWB amplitude is positively correlated with ε_z. Across our prior range, the GWB amplitude increases nearly linearly by approximately 2 orders of magnitude. Since model M_{ε} only sampled one parameter, there is very little spread in the light blue points (hence they appear as a line). The only difference between any two points with similar values of ε_z comes from the Poisson noise in HOLODECK.

The positive correlation between the GWB amplitude and ε_z is present in model $M_{\varepsilon+}$, although the spread in amplitude values is much larger than in model M_{ε}. The average standard deviation of $\log h_c$ is 0.022 for model M_{ε} and 1.13 for model $M_{\varepsilon+}$. Because model $M_{\varepsilon+}$ varied additional parameters to model M_{ε}, two points, with near identical values of ε_z, can have a wide range of other parameter values, and so the GWB amplitude for those two sample sets can differ. Therefore, the dark blue points deviate from the overall trend, because of the increased degrees of freedom in the model, but the median trend (blue squares) matches that of model M_{ε} very closely. Therefore, dependence on ε_z is present in model $M_{\varepsilon+}$, but much less direct, and so there is less reliance on ε_z to match the GWB compared with model M_{ε}. This same behavior affects the posterior distributions for ε_z. The posterior distribution for model M_{ε} is narrower and takes on higher values on average than that of model $M_{\varepsilon+}$. With multiple free parameters, model $M_{\varepsilon+}$ can produce a GWB spectrum consistent with the data with different combinations of parameters.

4.3. Model M_{α}: Including Multiple Types of M_{BH}–M_{bulge} Evolution

Our main focus in this paper is the M_{BH}–M_{bulge} intrinsic scatter, although it is possible that both the normalization and scatter of the M_{BH}–M_{bulge} are changing with time. In Section 3, we saw that changes to the normalization and scatter have different impacts on the shape of the GWB spectrum. It is therefore feasible that both types of evolution can provide better fits to the GWB than either one alone. It is also possible that we can differentiate between these models with the available data.

Though their effects are frequency-dependent, both α_z and ε_z generally scale positively with the GWB amplitude, so there is a negative correlation between these parameters in our models (correlation coefficient of -0.85). To mitigate the effect of this degeneracy, we choose to fix the ε_z parameter to a constant value of 0.5 while allowing α_z to vary. We inform this value of ε_z based on the posterior distribution of model $M_{\varepsilon+}$. This value of ε_z is high enough to be a significant evolution without being so high as to dominate the shape or amplitude of the GWB spectrum. This model we refer to as model M_{α}.

With this model, the posterior distribution for α_z (Figure 9) is 99.9% positive, with a median value of $\alpha_z = 0.84 \pm 0.35$. The associated best-fit spectrum is shown in Figure 2 (dark red dotted line). This spectrum is notably higher in amplitude than our ε_z-only model, but it is only minimally different from model $M_{\varepsilon+}$. The model M_{α} best-fit spectrum has a marginally stronger turnover, but overall the single α_z parameter has a similar overall effect to the combined impact of the eight additional free parameters in model $M_{\varepsilon+}$.

To compare the model fits, we calculate the linear Bayes factors between our models by marginalizing the likelihoods (calculated during fitting) over the prior distributions. In this case, model M_{α} is favored over both other models, though the preference is weak. The Bayes factor in favor of model M_{α} over model M_{ε}, calculated across the first 5 (11) frequency bins, is 2.17 (3.77), and the Bayes factor in favor of model M_{α} over model $M_{\varepsilon+}$ is 1.32 (3.02). The higher frequencies are where the effects of scatter and normalization evolution are most significantly different (e.g., Figure 1), therefore it makes sense that the Bayes factor between model $M_{\varepsilon+}$ and model M_{α} would change when including these higher frequencies. With

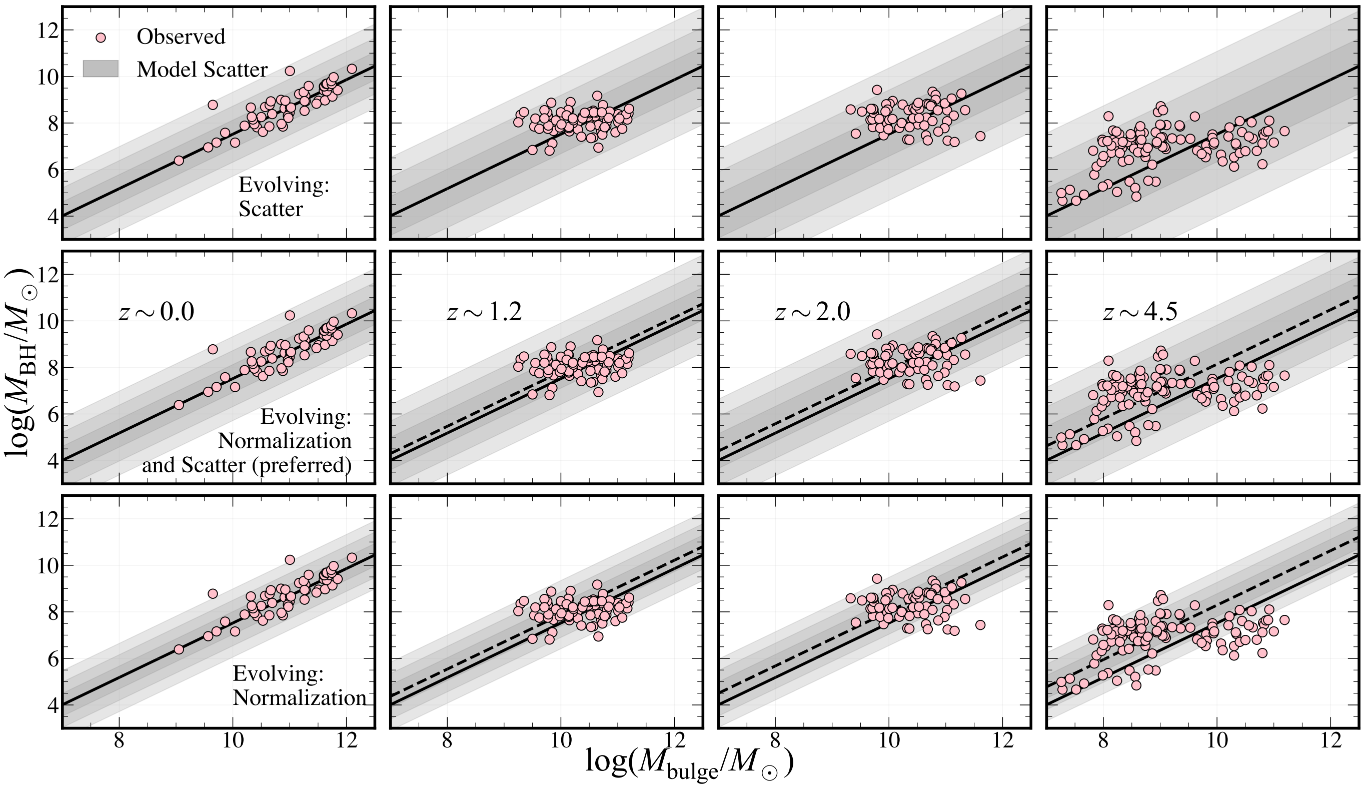

Figure 4. A comparison between our result predictions and the observed SMBH and galaxy masses. In gray, we show the 1σ, 2σ, and 3σ regions of scatter around the $M_{\rm BH}$–$M_{\rm bulge}$ relation from J. Kormendy & L. C. Ho (2013), with three different options for evolution. We add 0.4 dex in quadrature to the intrinsic scatter to approximate the measurement error. In all panels, the solid black line represents the local $M_{\rm BH}$–$M_{\rm bulge}$ relation, and the dashed line is the location of the evolving relation. The pink circles in each panel represent EM-observed SMBH–galaxy measurements from the literature. From left to right, we include data from J. Kormendy & L. C. Ho (2013), X. Ding et al. (2020), Y. Zhang et al. (2023), and the final panel includes data from Y. Sun et al. (2025b), J. Li et al. (2025a), B. L. Jones et al. (2025), and M. Brooks et al. (2026). Top row: the intrinsic scatter of the relation evolves according to the median posterior value from model M_ε, $\varepsilon_z = 1.05$. The normalization is unchanging. Middle row: both the intrinsic scatter and normalization are evolving according to the results from model M_α, $\varepsilon_z = 0.5$, $\alpha_z = 0.84$. Bottom row: only the normalization is evolving here. This represents the best-fit model from C. Matt et al. (2026), $\alpha_z = 1.04$. All three cases predict a population of overmassive SMBHs consistent with high-redshift JWST observations without violating local constraints. The two options with evolving scatter also predict an undermassive population, which can reproduce the "normal-mass" SMBHs found by J. Li et al. (2025a). This lower-mass population is not predicted by the high-normalization, low-scatter model.

more frequencies, the inclusion of an evolving $M_{\rm BH}$–$M_{\rm bulge}$ normalization becomes more important for reproducing the observed spectrum. The GWB data, however, are not well constrained beyond the first five frequency bins, so we cannot make strong conclusions based on these numbers. In the following section, we further evaluate these models in the context of additional EM data.

5. Comparisons to $M_{\rm BH}$–$M_{\rm bulge}$ Relations Measured across Cosmic Time

In previous sections, we showed that the GWB data alone may be able to break the degeneracy between types of $M_{\rm BH}$–$M_{\rm bulge}$ evolution with improvements to the constraints for high-frequency data. Here, we investigate how EM data may be able to provide independent constraints. EM-based studies of the $M_{\rm BH}$–$M_{\rm bulge}$ relation outside the local Universe exist across a wide range of redshifts. The sample size of observed SMBH–galaxy pairs decreases with increasing redshift, due to observational limitations. Now, several years after the launch of JWST, the field has amassed a decent sample of extremely high-redshift studies of the $M_{\rm BH}$–$M_{\rm bulge}$ relation. The picture of the $z > 4$ SMBH population is becoming increasingly complex, as some studies find SMBH–galaxy pairs that lie significantly above the local $M_{\rm BH}$–$M_{\rm bulge}$ relation (e.g., F. Pacucci et al. 2023; M. Yue et al. 2024), while others find pairs that are consistent with (or even below) local measurements (e.g, X. Ding et al. 2023; J. Li et al. 2025a; Y. Sun et al. 2025a). This diversity of mass ratios has intriguing implications for the model of SMBH–galaxy coevolution and suggests a wide variety of growth pathways. It additionally hints at possible observational biases that can lead to misinformed conclusions about the entire population. Whether these high-redshift massive SMBHs represent an overmassive population or the extreme end of a relation, they are not predicted by extrapolations of the local relation. A full analysis of the redshift evolution of the intrinsic scatter in the $M_{\rm BH}$–$M_{\rm bulge}$ relation using only EM data is outside the scope of this paper. Even a simple analysis, however, yields valuable insights. Here, we present a qualitative but robust comparison of the predictions from our results and various EM-based SMBH–galaxy mass measurements.

In Figure 4, we show the predicted $M_{\rm BH}$–$M_{\rm bulge}$ relation with intrinsic scatter that evolves according to our best-fit parameters. We are interested in distinguishing between these two evolutionary options. Previously, we demonstrated that different types of $M_{\rm BH}$–$M_{\rm bulge}$ evolution have different impacts on the GWB spectrum, which may someday be differentiable with GWB data alone. We now consider how EM-based measurements of SMBH and galaxy masses may be able to place independent and complementary constraints on this problem. For this purpose, we model the evolution of the intrinsic $M_{\rm BH}$–$M_{\rm bulge}$ relation in three cases: (i) a relation with strong scatter evolution, but no normalization evolution (top row, model M_{ε}); (ii) a relation with moderate evolution in both scatter and normalization (middle row, model M_{α}); and (iii) a relation with strong normalization evolution, but no scatter evolution (C. Matt et al. 2026) (bottom row). The gray regions in each panel are the 1σ, 2σ, and 3σ regions of the intrinsic scatter at that redshift (which is modeled by a normal distribution). Measurement errors on the SMBH masses inferred from the luminosity scaling relations cause the apparent $M_{\rm BH}$–$M_{\rm bulge}$ scatter to be greater than the intrinsic scatter (typically ranging form 0.2 to 0.6 dex, depending on the relation; e.g., M. Vestergaard & B. M. Peterson 2006; E. Dalla Bontà et al. 2025). We therefore add 0.4 dex in quadrature to the modeled intrinsic scatter to account for this. We additionally add the average stellar mass error (0.3 dex multiplied by the $M_{\rm BH}$–$M_{\rm bulge}$ slope) in quadrature. These errors are the average reported values across the studies we consider here.

Overlaid are a selection of observed EM-based SMBH–galaxy pairs with mass measurements from the literature. For all but the highest-redshift panel, we only compare our simulated population to one individual study per redshift bin. The data from X. Ding et al. (2020) and Y. Zhang et al. (2023) are each from a single survey, so we can ignore cross-study systematics that may otherwise artificially inflate the scatter of the relation in these bins. There are limited samples for $z > 4$, so we compile several datasets for our highest-redshift bin. We carefully select data from studies that combined several high-redshift SMBH–galaxy mass estimates and corrected for study systematics (J. Li et al. 2025a; Y. Sun et al. 2025b). We additionally include data from B. L. Jones et al. (2025) and M. Brooks et al. (2026). Except for M. Brooks et al. (2026), these studies all use similar methods for measuring SMBH and galaxy masses, e.g., a delayed-τ star formation history model, a Chabrier initial mass function (G. Chabrier 2003), and Hα-broadline-derived SMBH masses. We include the data from M. Brooks et al. (2026) to increase the completeness of our sample, but we recognize this may contaminate our scatter estimates for this bin.

In Figure 4, the two models with scatter evolution are more consistent with the EM data than the evolving-normalization-only model. This is especially apparent at higher redshifts; in the $z \sim 5.0$ panel, the model without increasing scatter fails to capture the normal- and lower-mass SMBH–galaxy pairs. While model M_{ε} previously was a relatively poor fit to the GWB spectrum, here it provides the best agreement with the EM datasets at all redshifts. The simulated population based on model $M_{\varepsilon+}$ predicts more overmassive and fewer under-massive SMBHs than we see in the data for $z \gtrsim 2.0$, though there are at least some SMBHs in every region where EM data are. The model without scatter evolution predicts nearly no SMBH–galaxy pairs below the local relation at $z \sim 5.0$. This model provides excellent fits to the GWB spectrum and, when only considering gravitational-wave data, is the best model (C. Matt et al. 2026). However, given that pairs have been electromagnetically observed to lie on and below the local relation in this redshift range, we conclude that this model is a poor description of all the available data.

In Figure 5, we show the predicted value of $\varepsilon(z)$ across redshift from each of our three models. We compare these to

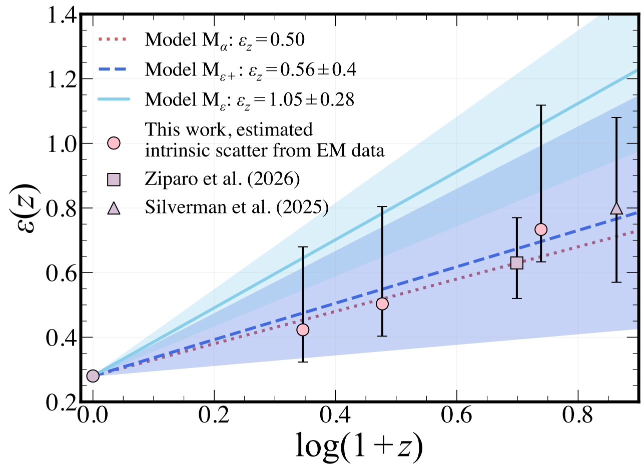

Figure 5. The value of the scatter in the $M_{\rm BH}$–$M_{\rm bulge}$ relation versus redshift for the data in Figure 4. The lines represent the predicted evolution of $\varepsilon(z)$ using the median of the posterior for ε_z in model M_{ε} (solid blue line), model $M_{\varepsilon+}$ (dashed blue line), and the fixed value in model M_{α} (dotted red line), with their 68% confidence intervals indicated by the shaded regions and in the caption. We estimate the intrinsic scatter of the EM data in our three nonlocal redshift bins by calculating the standard deviation of the vertical distance from the local J. Kormendy & L. C. Ho (2013) relation and subtracting the measurement error in quadrature (pink points). The lowest-redshift purple circle is the 0.28 dex value reported by J. Kormendy & L. C. Ho (2013). We additionally show two high-redshift scatter estimates from the literature as the purple square (F. Ziparo et al. 2026) and purple triangle (J. D. Silverman et al. 2025), respectively. The estimated and literature scatter values lie close to the model predictions from model $M_{\varepsilon+}$ and model M_{α}, indicating that a moderate scatter evolution is favored by the EM data over the strong evolution in model M_{ε}.

estimates of the intrinsic scatter in the three highest-redshift bins in Figure 4 (pink circles). Our model necessarily matches the J. Kormendy & L. C. Ho (2013) value (0.28 dex) at $z = 0$, which we show as the leftmost purple circle. We additionally show two measurements of the $M_{\rm BH}$–$M_{\rm bulge}$ scatter from the literature as the purple square (F. Ziparo et al. 2026) and purple triangle (J. D. Silverman et al. 2025), respectively. We note that the data in F. Ziparo et al. (2026) are reported to lie at $z \gtrsim 4$ and we place the square at $z = 4$ in this plot. We measure the total scatter, $\sigma_{\rm tot}$, of the EM data as the standard deviation of the difference between the reported SMBH mass and the local $M_{\rm BH}$–$M_{\rm bulge}$ relation. To estimate the intrinsic scatter, we subtract the SMBH mass and galaxy stellar/bulge mass measurement error from the total scatter in quadrature. Specifically, we calculate $\sigma^2_{\rm intrinsic} = \sigma^2_{\rm tot} - M^2_{\rm BH,err} - (M_{\rm stellar,err}\beta_0)^2$, where β_0 is the local slope of the $M_{\rm BH}$–$M_{\rm bulge}$ relation. For each study, we take the average reported error, if the errors are different for each object, but consider the full range in our uncertainties. We do not have bulge masses for the two highest-redshift bins. We test the effect of the bulge fraction uncertainty by measuring the scatter of a simulated sample of galaxies with bulge fractions drawn from a uniform distribution. With a lower limit on the bulge fraction of 15%, we determine the typical effect is to inflate the inferred scatter by ~0.1 dex, so we lower the $\sigma_{\rm intrinsic}$ estimate by 0.1 dex in both bins. To account for unknown systematics and the large uncertainties in the stellar mass estimates for B. L. Jones et al. (2025), we additionally subtract off 0.15 dex from $\sigma_{\rm intrinsic}$ in the highest-redshift bin. This value is motivated by the total spread in the individually measured scatters for each study. We find the difference between the highest and lowest individual scatter to be ~0.3 dex, so we subtract off 0.15 dex to accommodate this uncertainty. This

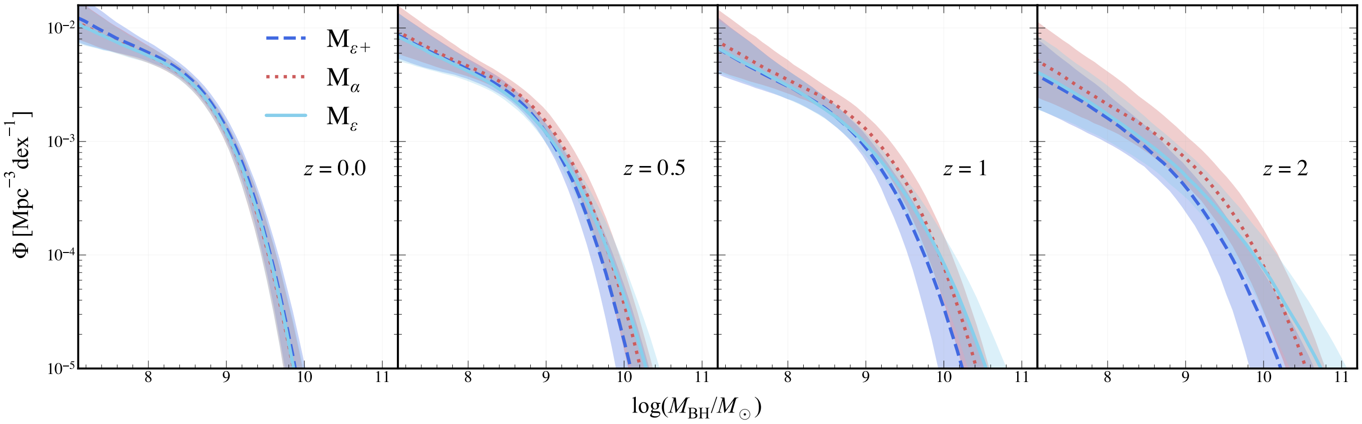

Figure 6. The BHMFs associated with the GWB spectrum best-fit parameters for our models. The solid light blue BHMF represents our model that samples only the scatter evolution parameter, model M_ε. The darker blue dashed line represents model $M_{\varepsilon+}$ and the red dotted line is model M_α. Locally, all three models with evolving scatter are identical by design. Both BHMFs from model M_ε and model M_α track each other nearly identically at each redshift, with model M_α having very slightly higher number densities of $M_{\rm BH} \lesssim 10^{10}\,M_\odot$. Especially at the highest redshifts, the BHMF from model $M_{\varepsilon+}$ is generally below all others. This model has a higher GWB amplitude than model M_ε but lower SMBH number densities nearly everywhere. The additional parameters in model $M_{\varepsilon+}$, such as the hardening timescales, affect the GWB amplitude, but are not reflected in the BHMF. The value of ε_z is similar between $M_{\varepsilon+}$ and model M_α, but the BHMF for model M_α is more similar to that of model M_ε, because the α_z parameter increases the GWB amplitude via increasing the SMBH number density.

large range in scatter estimates is impacted by the fact that the sample from B. L. Jones et al. (2025) is made up of 43% of little red dots. The stellar and BH mass estimates for these objects are highly uncertain, so while we include these data for completeness, we acknowledge that they increase the uncertainty in our scatter measurement in the highest-redshift bin. None of the other studies we consider include little red dots in their sample. The upper limits of our error bars represent the standard deviation of the data before taking any errors into account. The lower limits come from our scatter estimates in the most conservative case, for what we assume as errors on the mass measurements and bulge fraction uncertainties. We see that the EM-based trend is most similar to the models with more moderate evolution: model $M_{\varepsilon+}$ and model M_α.

This semiqualitative comparison demonstrates the power of a multimessenger analysis. We show that an $M_{\rm BH}$–$M_{\rm bulge}$ relation with evolving intrinsic scatter provides better fits to the EM data than models with no scatter evolution. When fitting the GWB data, we find that models without $M_{\rm BH}$–$M_{\rm bulge}$ normalization fail to recover both the amplitude and shape of the spectrum. Models with evolving normalization only can reproduce the GWB data, but fail to match the EM observations. Including both normalization and scatter evolution provides decent fits to the GWB data and makes predictions compatible with EM observations. We therefore conclude that an $M_{\rm BH}$–$M_{\rm bulge}$ relation that evolves moderately in both normalization and scatter provides the best single model of all available data.

It has been known and discussed for many years that magnitude-limited surveys can bias analyses of the $M_{\rm BH}$–$M_{\rm bulge}$ relation toward higher normalizations and shallower slopes (T. R. Lauer et al. 2007). In other words, a population of SMBHs and galaxies that follows a high-scatter $M_{\rm BH}$–$M_{\rm bulge}$ relation can appear to follow a higher-normalization $M_{\rm BH}$–$M_{\rm bulge}$ relation when sampled with a magnitude-limited survey. Our results suggest that the amplitude of the normalization offset observed at $z > 4$ may not be as large as reported in some of the earlier JWST results (F. Pacucci et al. 2023); however, the GWB data do support a nonnegligible positive normalization offset. It remains challenging to disentangle systematic and observational biases from the EM data. As more surveys begin probing the lower SMBH mass and lower SMBH–galaxy mass ratio regimes, a dedicated EM-based study of the intrinsic scatter at high redshift is necessary (J. D. Silverman et al. 2025; F. Ziparo et al. 2026).

6. BH Number Density

The observable nanohertz GWB amplitude is determined from the number of SMBH binaries emitting gravitational waves in the PTA regime. From our fits, we can calculate the implied total SMBH mass distribution that describes the GWB. In Figure 6, we show the BHMFs associated with each of our best-fit models. Necessarily, all three BHMFs from our evolving models are equivalent at $z = 0$. We do not see noticeable differences until $z > 1$, where the BHMFs from model M_ε and model M_α have similar number densities to each other, but both are higher than the model $M_{\varepsilon+}$ BHMF. Though the difference appears only slight, the increased number density for $M_{\rm BH} \lesssim 10^{10}\,M_\odot$ seen in model M_α leads to the higher GWB spectrum amplitude in model M_α versus model M_ε in Figure 2. This effect is the same as demonstrated in Figure 1 and discussed in Section 3.

We consider an additional test case of a model that does not allow for scatter evolution and instead only samples the local scatter value. It is important to note that this test case is ruled out by the constraints on the local intrinsic scatter, but it is useful to consider the differences between evolving and nonevolving scatter. We compare this model with model M_ε in Figure 7. Increasing the local scatter matches the GWB just as well as evolving scatter. At $z = 0$, the BHMFs are very different, with the locally increased scatter BHMF having a number density over 10 times higher than model M_ε for $M_{\rm BH} > 10^{10}\,M_\odot$. This difference is less significant for higher redshifts, where the BHMFs are roughly consistent for $z > 1$.

7. Discussion

An evolving relationship between the SMBH and galaxy bulge mass offers a promising explanation that can unify EM observations at high and low redshift with gravitational-wave data. In this work, we focus on the impact of an evolving intrinsic scatter in the $M_{\rm BH}$–$M_{\rm bulge}$ relation on predicted

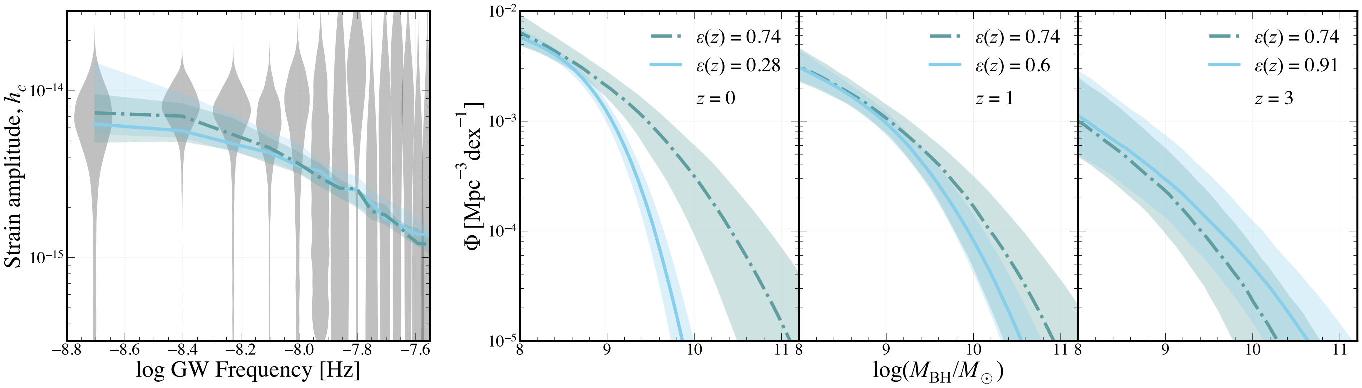

Figure 7. A comparison between the best-fit spectra and associated BHMFs from model M_ε (solid line) and a model with nonevolving but increased scatter (dotted–dashed line). The BHMF from model M_ε is the same as in Figure 6. In the upper right, we show the value of the intrinsic scatter for each model at the relevant redshift; only the value associated with model M_ε changes, since the other is nonevolving.

SMBH populations and the predicted GWB. Our results show that a high scatter outside the local Universe predicts a population of SMBHs that can produce a GWB amplitude consistent with the observed NANOGrav spectrum, while also matching the high-redshift “overmassive” SMBH population observed by JWST surveys. Our high-scatter models additionally predict an unobserved population of “undermassive” BHs that mirror the “overmassive” population.

A significant number of SMBH masses measured at $z > 4$ from JWST surveys lie significantly above the local $M_{\rm BH}$–$M_{\rm bulge}$ relation (e.g., Y. Harikane et al. 2023; F. Pacucci et al. 2023; H. Übler et al. 2023; R. Maiolino et al. 2024; M. A. Stone et al. 2024; M. Yue et al. 2024), even after mass corrections (J. Li et al. 2025b; Y. Sun et al. 2025b). However, several studies have claimed that these objects, while real, are not representative of the underlying population and are instead results of magnitude-limited surveys failing to detect normal and undermassive SMBH–galaxy pairs (J. Li et al. 2025b; J. D. Silverman et al. 2025; F. Ziparo et al. 2026). Indeed, there have been some recent results showing that there may exist a population of SMBHs that are not overmassive relative to their hosts (e.g., X. Ding et al. 2023; J. Li et al. 2025a; M. Brooks et al. 2026; S. Geris et al. 2026). Neither the local relation nor a high-normalization relation can explain these results. The local relation will underpredict the overmassive SMBH–galaxy pairs, while an evolving normalization cannot reproduce the “normal”-mass pairs. An evolving intrinsic scatter, however, predicts a large spread in mass ratios, which predicts the overmassive, normal-mass, and undermassive populations.

An intrinsic scatter that is greater in the past and lower at the present day has several physical interpretations. It could imply that the local correlation between SMBH mass and galaxy mass is noncausal, being instead a natural outcome of galaxy and SMBH mergers (e.g., C. Y. Peng 2007; M. Hirschmann et al. 2010; K. Jahnke & A. V. Macciò 2011; H. Hu et al. 2025). Alternatively, the intrinsic scatter at high redshift could carry information about SMBH seeding and feedback interactions during SMBH and galaxy growth (J. E. Greene et al. 2020; M.-Y. Zhuang & L. C. Ho 2023; B. A. Terrazas et al. 2025). A high normalization suggests that SMBHs are born from heavy seeds, but a high scatter would suggest multiple seeding pathways are viable. A scatter that decreases with time could indicate that there is a diversity of growth pathways for SMBH–galaxy pairs. In some cases, SMBH growth may drastically outpace the host, where feedback from SMBH accretion can suppress star formation, delaying stellar mass growth and leading to a high $M_{\rm BH}/M_{\rm bulge}$ ratio early on. Eventually, the galaxy must be able to grow its mass without significant change to the SMBH mass, such that the $M_{\rm BH}/M_{\rm bulge}$ ratio reaches the value we observe today. Conversely, the galaxy may grow first and UV radiation from star formation can prevent gas from reaching the Galactic Center, postponing SMBH accretion and leading to an initially low $M_{\rm BH}/M_{\rm bulge}$ ratio. A high scatter implies that both of these feedback interactions may be present in different SMBH–galaxy pairs, rather than one dominating over the other on a population level (which could instead present as a high/low $M_{\rm BH}$–$M_{\rm bulge}$ normalization in the past).

It has been suggested that active SMBHs may follow a different host–mass relationship than inactive SMBHs (e.g., A. E. Reines & M. Volonteri 2015; J. E. Greene et al. 2020). Our model does not differentiate between active and quiescent SMBHs. If these populations indeed follow different relations, then, observationally, two (or more) low-scatter relations could blend together to appear as one with higher scatter. Our test that sampled only the local intrinsic scatter provided similarly good fits to the GWB data as the evolving scatter model, but implied a large number of local overmassive SMBHs. With a high intrinsic scatter, the most massive SMBHs need not exist exclusively in massive galaxies, and so we would expect to have observed this overmassive population by now with large local surveys.

Due to Eddington bias, the impact of this evolving scatter is greatest for the high-mass end of the BHMF. Therefore, this high-scatter $M_{\rm BH}$–$M_{\rm bulge}$ relation does not significantly change the number density of SMBHs with masses $M_{\rm BH} < 10^9\,M_\odot$. The impact on the GWB amplitude is therefore negligible for frequencies $f_{\rm gw} \gtrsim 10$ nHz. From the GWB side, we do not see statistical preference for evolving normalization versus scatter. There is strong evidence to support evolving normalization being the best fit to the GWB data, but it produces a poor model for the EM data, so there is either a large discrepancy here or the GWB data are not yet at the point where we can discern between these options.

This work demonstrates the need for improving the precision of GWB data and for increasing the available EM data. Analyses of the GWB can eventually be used to differentiate between different SMBH population models, but are currently limited by the number of reliable frequency bins.

Future gravitational-wave data releases with well-constrained high-frequency data will greatly improve our ability to distinguish between the effects of $M_{\rm BH}$–$M_{\rm bulge}$ scatter and normalization. Furthermore, it is important to perform dedicated statistical analyses of the available EM data, to evaluate the effects of observational bias as well as the impacts of assumptions made between papers (J. D. Silverman et al. 2025; F. Ziparo et al. 2026).

The models we present here indicate that an $M_{\rm BH}$–$M_{\rm bulge}$ relation that evolves both in scatter and normalization provides better fits than either type of individual evolution. A relation that is large in scatter and minimally offset in normalization would be difficult to confirm observationally. Some studies have made great efforts to remove any possible observational bias from their data to measure an intrinsic $M_{\rm BH}$–$M_{\rm bulge}$ normalization offset, though the results of these analyses can yield conflicting results. For example, Y. Zhang et al. (2023) find a $\sim$0.52 dex increased $M_{\rm BH}/M_\star$ ratio at $z \sim 2$, whereas Y. Sun et al. (2025b) find their $M_{\rm BH}/M_\star$ ratio to be consistent with the local value.

If the $M_{\rm BH}$–$M_{\rm bulge}$ relation is changing with time, in any way, it is imperative that we constrain its functional form. The consequences of misestimating the SMBH population at high redshift extend beyond gravitational-wave studies. Other relations, such as the $M_{\rm BH}$–σ relation, predict different SMBH masses at high z and may be relatively unchanging with time (e.g., C. Matt et al. 2023; J. Simon 2023; J. H. Cohn et al. 2025; M. C. Huber et al. 2025). Eventually, the GWB can and should be used to test alternative relationships against each other.

8. Summary

We have used a semianalytic model to synthesize populations of SMBH binaries and calculate the resulting GWB. We have tested the predictions from different versions of the $M_{\rm BH}$–$M_{\rm bulge}$ scaling relation against the NANOGrav 15 yr GWB spectrum and EM observational data and placed constraints on how this relationship may be changing with time. Our results suggest that the intrinsic scatter of the $M_{\rm BH}$–$M_{\rm bulge}$ relation, measured locally to be 0.28 dex, must have been higher in the past. A larger intrinsic scatter at high redshift ($\sim$0.7 dex by $z \sim 5$) predicts a large population of SMBHs with masses well above the $M_{\rm BH}$–$M_{\rm bulge}$ relation. This population produces a GWB higher in amplitude than predicted from a nonevolving $M_{\rm BH}$–$M_{\rm bulge}$ relation, though this amplitude increase is negligible for the highest frequencies. At this point in time, the data are not reliable for frequencies higher than $f \sim 10$ nHz, so we cannot determine the validity of the lack of amplitude increase in this regime. A high intrinsic scatter can explain the population of overmassive SMBHs found in various JWST observations, and predicts a population of SMBHs with masses both on and far below the local relation that is not yet observed.

We have considered the different impacts between evolving normalization and scatter. We find that both an evolving normalization and scatter provide a better fit to the GWB data than only evolving scatter, and this is not ruled out by the EM observations. Considering the population of SMBHs at $z > 4$ we use here (B. L. Jones et al. 2025; J. Li et al. 2025a; Y. Sun et al. 2025b; M. Brooks et al. 2026), a low-scatter, high-normalization $M_{\rm BH}$–$M_{\rm bulge}$ relation fails to predict the underlying SMBH population at high redshifts, despite being a great fit to the GWB data. We therefore conclude that the intrinsic scatter of the $M_{\rm BH}$–$M_{\rm bulge}$ relation must be higher in the past to explain high-redshift EM observations, and the normalization must have been higher to explain the gravitational-wave data.

Acknowledgments

C.M. is grateful for support from a Frontera Computational Science Fellowship and computational resources from the Texas Advanced Computing Center at the University of Texas at Austin. The authors would like to thank Jinyi Yang and Feige Wang for helpful discussions. The authors also wish to thank the anonymous referee for the thoughtful review and suggestions. L.B. acknowledges support from the National Science Foundation under award AST-2307171 and from the National Aeronautics and Space Administration under award 80NSSC22K0808. P.R.B. is supported by the Science and Technology Facilities Council, grant No. ST/W000946/1. S.B. gratefully acknowledges the support of a Sloan Fellowship and the support of NSF under award No. 1815664. The work of R.B., R.C., X.S., J.T., and D.W. is partly supported by the George and Hannah Bolinger Memorial Fund in the College of Science at Oregon State University. M.C. acknowledges support by the European Union (ERC, MMMonsters, 101117624). Support for this work was provided by the NSF through the Grote Reber Fellowship Program administered by Associated Universities, Inc./National Radio Astronomy Observatory. H.T.C. acknowledges funding from the U.S. Naval Research Laboratory. Pulsar research at UBC is supported by an NSERC Discovery Grant and by CIFAR. K.C. is supported by a UBC Four Year Fellowship (6456). M.E.D. acknowledges support from the Naval Research Laboratory by NASA under contract S-15633Y. T.D. and M.T.L. received support from NSF Astronomy and Astrophysics Grant (AAG) award No. 2009468 during this work. E.C.F. is supported by NASA under award No. 80GSFC24M0006. K.A.G. and S.R.T. acknowledge support from NSF CAREER award No. 2146016. D.C.G. is supported by NSF Astronomy and Astrophysics Grant (AAG) award No. 2406919. A.D.J. acknowledges support from the Caltech and Jet Propulsion Laboratory President's and Director's Research and Development Fund. A.D.J. acknowledges support from the Sloan Foundation. N.La. was supported by the Vanderbilt Initiative in Data Intensive Astrophysics (VIDA) Fellowship. Part of this research was carried out at the Jet Propulsion Laboratory, California Institute of Technology, under a contract with the National Aeronautics and Space Administration (80NM0018D0004). D.R.L. and M.A.M. are supported by NSF No. 1458952. M.A.M. is supported by NSF No. 2009425. C.M.F.M. was supported in part by the National Science Foundation under grant Nos. NSF PHY-1748958 and AST-2106552. A.Mi. acknowledges support from a Royal Society University Research Fellowship (URF-R1-251896). The Dunlap Institute is funded by an endowment established by the David Dunlap family and the University of Toronto. K.D.O. was supported in part by NSF grant No. 2207267. T.T.P. acknowledges support from the Extragalactic Astrophysics Research Group at Eötvös Loránd University, funded by the Eötvös Loránd Research Network (ELKH), which was used during the development of this research. P.P. and S.R.T. acknowledge support from NSF AST-2007993. H.A.R. is supported by NSF Partnerships for Research and Education in Physics (PREP) award No. 2216793. S.M.R. and I.H.S. are CIFAR Fellows. Portions of this work performed at NRL were supported by ONR 6.1 basic research funding. J.D.R. also acknowledges support from start-up funds from Texas Tech University. S.C.S. and S.J.V. are supported by NSF award PHY-2011772. J.S. is supported by an NSF Astronomy and Astrophysics Postdoctoral Fellowship under award AST-2202388 and acknowledges previous support by the NSF under award 1847938. O.Y. is supported by the National Science Foundation Graduate Research Fellowship under grant No. DGE-2139292.

Anishinaabeg gaa bi dinokiiwaad temigad manda Michigan Kichi Kinoomaagegamig. Mdaaswi nshwaaswaak shi mdaaswi shi niizhawaaswi gii-sababoonagak, Ojibweg, Odawaag, minwaa Bodwe'aadamiig wiiba gii-miigwenaa'aa maamoonjiniibina Kichi Kinoomaagegamigoong wi pii-gaa aanjibiigaadeg Kichi-Naakonigewinning, debendang manda aki, mampii Niisaajiwan, gewiinwaa niijaansiwaan ji kinoomaagaazinid. Daapanaming ninda kidwinan, megwaa minwaa gaa bi aankoosejig zhinda akiing minwaa gii-miigwewaad Kichi-Kinoomaagegamigoong aanji-daapinanigaade minwaa mshkowenjigaade.

The University of Michigan is located on the traditional territory of the Anishinaabe people. In 1817, the Ojibwe, Odawa, and Bodewadami Nations made the largest single land transfer to the University of Michigan. This was offered ceremonially as a gift through the Treaty at the Foot of the Rapids so that their children could be educated. Through these words of acknowledgment, their contemporary and ancestral ties to the land and their contributions to the University are renewed and reaffirmed.

Author Contributions

C.M. led the analysis and investigation of this project, as well as the writing and editing of this manuscript, and produced all figures and models. C.M. and K.G. were responsible for the conceptualization and supervision of this work. K.G. provided useful feedback and comments on the manuscript and aided in the scientific interpretation of the results. Additional NANOGrav members are listed in alphabetical order. Each contributed toward the collaboration-wide endeavor of pulsar timing that culminated in evidence for the GWB. The work presented in this paper benefits from data collected and analyzed in the course of this search and would not be possible without this large-scale coordination.

Appendix

Here, we include the posteriors for the parameters in model $M_{\varepsilon+}$ and model M_α that were not discussed in the main text. The posterior for ε_z from model $M_{\varepsilon+}$ is shown in the lower-right panel of Figure 8; this is the same distribution as seen previously in Figure 2.

In Figure 8, we see that the posterior distributions (blue solid lines) are nearly identical to the priors (gray dashed lines) for all our Gaussian priors. These priors are based on EM observations for the local GSMF ($\log \phi_{*,1,0}$, $\log \phi_{*,2,0}$, and $M_{c,0}$; J. Leja et al. 2020) and the $M_{\rm BH}$–$M_{\rm bulge}$ relation (α_0 and β_0; J. Kormendy & L. C. Ho 2013). The fact that the posteriors recover the priors here indicates that this model is in good agreement with EM observational constraints.

All three of the SMBH binary hardening parameters push against their prior bounds. The lower limit on the hardening timescale, τ_f, is 0 Gyr, and low values of this parameter were also seen by G. Agazie et al. (2023b). $\nu_{\rm inner}$ is the slope of the power law associated with the stellar scattering. The posterior returns low values, but the lower bound, -2, is sufficiently small to minimize that term, and lowering this bound has no significant effect. Finally, $R_{\rm char}$ indicates the point at which the BH binary hardening transitions from dynamical friction into stellar scattering. The physically motivated value is on the order of 10 pc (L. Z. Kelley et al. 2017). Our prior range is 2–20 pc, and the posterior distribution returns high values within this range. There is a degeneracy between $R_{\rm char}$ and $\nu_{\rm inner}$. When we allow $R_{\rm char}$ to go much higher, $\nu_{\rm inner}$ also returns higher values. For example, G. Agazie et al. (2023b) used a fixed value of $R_{\rm char} = 100$ pc and they found $\nu_{\rm inner} = -0.5$. The difference between these results is interesting and has been the focus of other studies (e.g., C. J. Harris et al. 2026), but does not have a significant impact on our conclusions about the redshift evolution of the $M_{\rm BH}$–$M_{\rm bulge}$ relation.

The posterior distribution for α_z from model M_α is shown in Figure 9. The shape is apparently Gaussian and has a median value of $\alpha_z = 0.84 \pm 0.35$. The distribution is 99.9% positive, indicating a strong preference for positive $M_{\rm BH}$–$M_{\rm bulge}$ normalization evolution. This model sampled only α_z and had all other parameters fixed to their fiducial values, except $\varepsilon_z = 0.5$. This evolution is a moderately good model for both the GWB and EM datasets we consider.

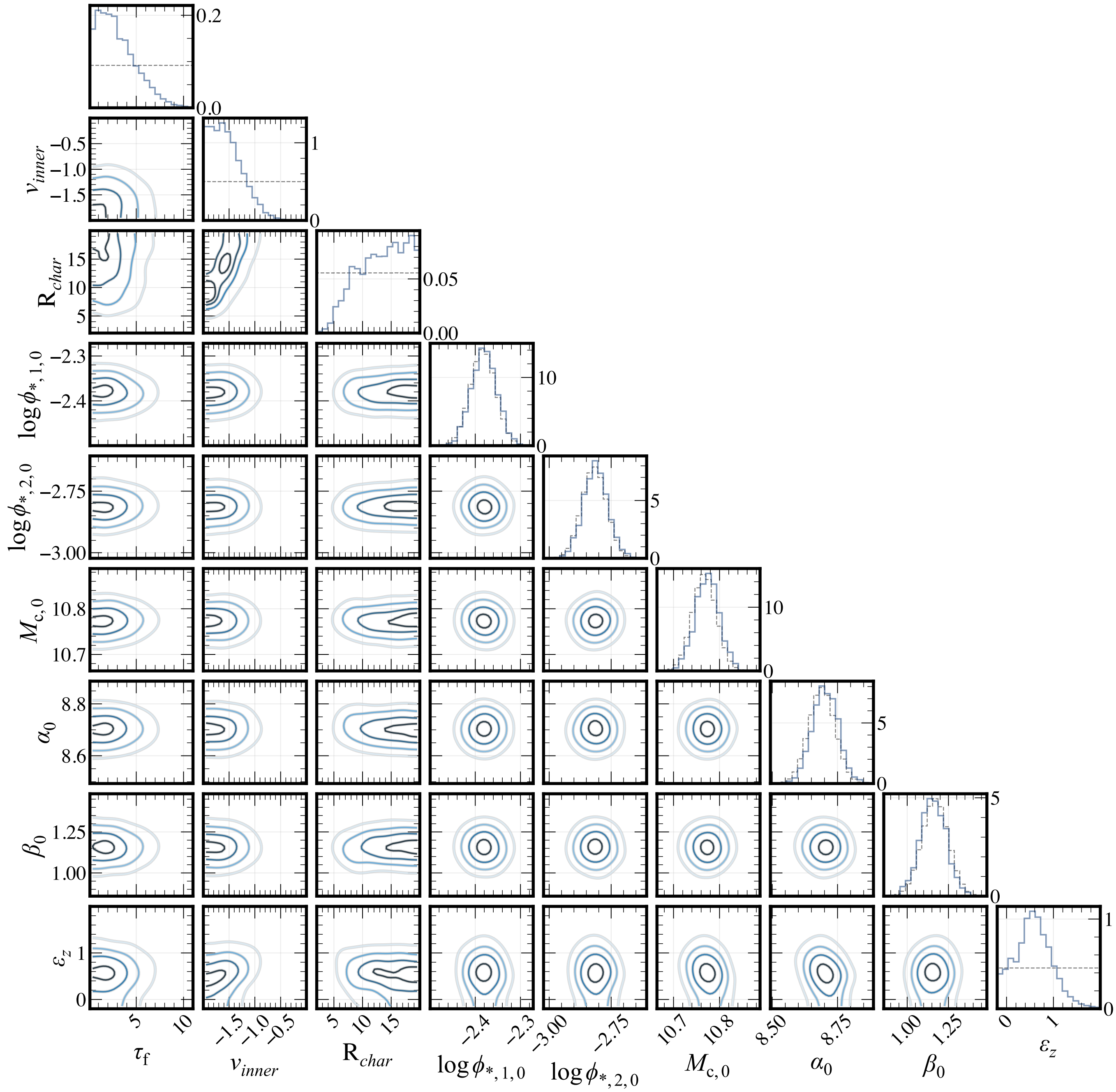

Figure 8. Corner plot of posteriors from model $M_{\varepsilon+}$. The posterior for ε_z is additionally shown in Figure 2.

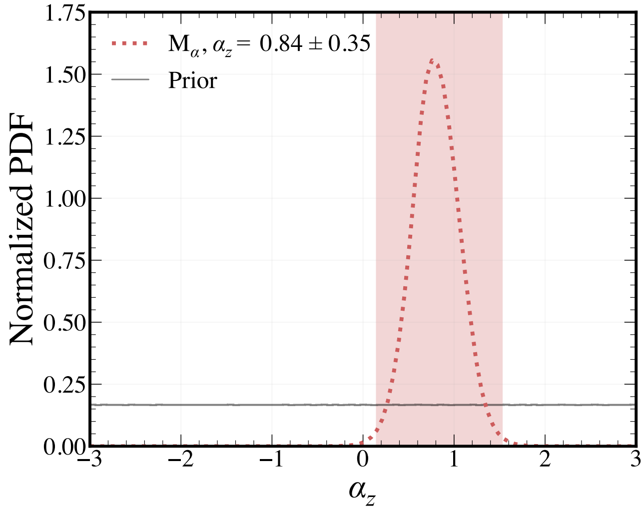

Figure 9. Histogram of the posterior for α_z in model M_α. The red shaded region shows the 68% confidence interval, and the horizontal gray line represents the uniform prior $-3.0 < \alpha_z < 3.0$. This was the only free parameter in this model. All other parameters were fixed to their fiducial values, except ε_z, which was fixed to 0.5.

ORCID iDs

Cayenne Matt https://orcid.org/0000-0002-9710-6527
Kayhan Gültekin https://orcid.org/0000-0002-1146-0198
Gabriella Agazie https://orcid.org/0000-0001-5134-3925
Akash Anumarlapudi https://orcid.org/0000-0002-8935-9882
Anne M. Archibald https://orcid.org/0000-0003-0638-3340
Zaven Arzoumanian https://orcid.org/0009-0008-6187-8753
Jeremy G. Baier https://orcid.org/0000-0002-4972-1525
Paul T. Baker https://orcid.org/0000-0003-2745-753X
Bence Bécsy https://orcid.org/0000-0003-0909-5563
Laura Blecha https://orcid.org/0000-0002-2183-1087
Adam Brazier https://orcid.org/0000-0001-6341-7178
Paul R. Brook https://orcid.org/0000-0003-3053-6538
Sarah Burke-Spolaor https://orcid.org/0000-0003-4052-7838
Rand Burnette https://orcid.org/0009-0008-3649-0618
J. Andrew Casey-Clyde https://orcid.org/0000-0002-5557-4007
Maria Charisi https://orcid.org/0000-0003-3579-2522
Shami Chatterjee https://orcid.org/0000-0002-2878-1502
Tyler Cohen https://orcid.org/0000-0001-7587-5483
James M. Cordes https://orcid.org/0000-0002-4049-1882
Neil J. Cornish https://orcid.org/0000-0002-7435-0869
Fronefield Crawford https://orcid.org/0000-0002-2578-0360
H. Thankful Cromartie https://orcid.org/0000-0002-6039-692X
Kathryn Crowter https://orcid.org/0000-0002-1529-5169
Megan E. DeCesar https://orcid.org/0000-0002-2185-1790
Paul B. Demorest https://orcid.org/0000-0002-6664-965X
Heling Deng https://orcid.org/0000-0002-1918-5477
Lankeswar Dey https://orcid.org/0000-0002-2554-0674
Timothy Dolch https://orcid.org/0000-0001-8885-6388
Graham M. Doskoch https://orcid.org/0000-0002-4219-6908
Elizabeth C. Ferrara https://orcid.org/0000-0001-7828-7708
William Fiore https://orcid.org/0000-0001-5645-5336
Emmanuel Fonseca https://orcid.org/0000-0001-8384-5049
Gabriel E. Freedman https://orcid.org/0000-0001-7624-4616
Emiko C. Gardiner https://orcid.org/0000-0002-8857-613X
Nate Garver-Daniels https://orcid.org/0000-0001-6166-9646
Peter A. Gentile https://orcid.org/0000-0001-8158-683X
Kyle A. Gersbach https://orcid.org/0009-0009-5393-0141
Joseph Glaser https://orcid.org/0000-0003-4090-9780
Deborah C. Good https://orcid.org/0000-0003-1884-348X
C. J. Harris https://orcid.org/0000-0002-4231-7802
Jeffrey S. Hazboun https://orcid.org/0000-0003-2742-3321
Ross J. Jennings https://orcid.org/0000-0003-1082-2342
Aaron D. Johnson https://orcid.org/0000-0002-7445-8423
Megan L. Jones https://orcid.org/0000-0001-6607-3710
David L. Kaplan https://orcid.org/0000-0001-6295-2881
Luke Zoltan Kelley https://orcid.org/0000-0002-6625-6450
Matthew Kerr https://orcid.org/0000-0002-0893-4073
Joey S. Key https://orcid.org/0000-0003-0123-7600
Nima Laal https://orcid.org/0000-0002-9197-7604
Michael T. Lam https://orcid.org/0000-0003-0721-651X
William G. Lamb https://orcid.org/0000-0003-1096-4156
Bjorn Larsen https://orcid.org/0000-0001-6436-8216
Natalia Lewandowska https://orcid.org/0000-0003-0771-6581
Tingting Liu https://orcid.org/0000-0001-5766-4287
Duncan R. Lorimer https://orcid.org/0000-0003-1301-966X
Jing Luo https://orcid.org/0000-0001-5373-5914
Ryan S. Lynch https://orcid.org/0000-0001-5229-7430
Chung-Pei Ma https://orcid.org/0000-0002-4430-102X
Dustin R. Madison https://orcid.org/0000-0003-2285-0404
Alexander McEwen https://orcid.org/0000-0001-5481-7559
James W. McKee https://orcid.org/0000-0002-2885-8485
Maura A. McLaughlin https://orcid.org/0000-0001-7697-7422
Natasha McMann https://orcid.org/0000-0002-4642-1260
Bradley W. Meyers https://orcid.org/0000-0001-8845-1225
Patrick M. Meyers https://orcid.org/0000-0002-2689-0190
Chiara M. F. Mingarelli https://orcid.org/0000-0002-4307-1322
Andrea Mitridate https://orcid.org/0000-0003-2898-5844
Cherry Ng https://orcid.org/0000-0002-3616-5160
David J. Nice https://orcid.org/0000-0002-6709-2566
Stella Koch Ocker https://orcid.org/0000-0002-4941-5333
Ken D. Olum https://orcid.org/0000-0002-2027-3714
Timothy T. Pennucci https://orcid.org/0000-0001-5465-2889
Benetge B. P. Perera https://orcid.org/0000-0002-8509-5947
Polina Petrov https://orcid.org/0000-0001-5681-4319
Nihan S. Pol https://orcid.org/0000-0002-8826-1285
Henri A. Radovan https://orcid.org/0000-0002-2074-4360
Scott M. Ransom https://orcid.org/0000-0001-5799-9714

Paul S. Ray https://orcid.org/0000-0002-5297-5278
Joseph D. Romano https://orcid.org/0000-0003-4915-3246
Jessie C. Runnoe https://orcid.org/0000-0001-8557-2822
Alexander Saffer https://orcid.org/0000-0001-7832-9066
Shashwat C. Sardesai https://orcid.org/0009-0006-5476-3603
Ann Schmiedekamp https://orcid.org/0000-0003-4391-936X
Carl Schmiedekamp https://orcid.org/0000-0002-1283-2184
Kai Schmitz https://orcid.org/0000-0003-2807-6472
Brent J. Shapiro-Albert https://orcid.org/0000-0002-7283-1124
Xavier Siemens https://orcid.org/0000-0002-7778-2990
Joseph Simon https://orcid.org/0000-0003-1407-6607
Sophia V. Sosa Fiscella https://orcid.org/0000-0002-5176-2924
Ingrid H. Stairs https://orcid.org/0000-0001-9784-8670
Daniel R. Stinebring https://orcid.org/0000-0002-1797-3277
Kevin Stovall https://orcid.org/0000-0002-7261-594X
Abhimanyu Susobhanan https://orcid.org/0000-0002-2820-0931
Joseph K. Swiggum https://orcid.org/0000-0002-1075-3837
Jacob Taylor https://orcid.org/0000-0001-9118-5589
Stephen R. Taylor https://orcid.org/0000-0003-0264-1453
Mercedes S. Thompson https://orcid.org/0009-0001-5938-5000
Jacob E. Turner https://orcid.org/0000-0002-2451-7288
Michele Vallisneri https://orcid.org/0000-0002-4162-0033
Rutger van Haasteren https://orcid.org/0000-0002-6428-2620
Sarah J. Vigeland https://orcid.org/0000-0003-4700-9072
Haley M. Wahl https://orcid.org/0000-0001-9678-0299
Kevin P. Wilson https://orcid.org/0000-0003-4231-2822
Caitlin A. Witt https://orcid.org/0000-0002-6020-9274
David Wright https://orcid.org/0000-0003-1562-4679
Olivia Young https://orcid.org/0000-0002-0883-0688

References

Agazie, G., Anumarlapudi, A., Archibald, A. M., et al. 2023a, ApJL, 951, L8
Agazie, G., Anumarlapudi, A., Archibald, A. M., et al. 2023b, ApJL, 952, L37
Bonoli, S., Izquierdo-Villalba, D., Spinoso, D., et al. 2025, arXiv:2509.12325
Brooks, M., Trump, J. R., Simons, R. C., et al. 2026, ApJ, 1002, 129
Chabrier, G. 2003, PASP, 115, 763
Chen, Y., Yu, Q., & Lu, Y. 2024, ApJ, 974, 261
Cohn, J. H., Durodola, E., Casey, Q. O., Lambrides, E., & Hickox, R. C. 2025, ApJL, 988, L61
Dalla Bontà, E., Peterson, B. M., Grier, C. J., et al. 2025, A&A, 696, A48
Dattathri, S., Natarajan, P., Porras-Valverde, A. J., et al. 2025, ApJ, 984, 122
Ding, X., Silverman, J., Treu, T., et al. 2020, ApJ, 888, 37
Ding, X., Onoue, M., Silverman, J. D., et al. 2023, Natur, 621, 51
Eddington, A. S. 1913, MNRAS, 73, 359
EPTA CollaborationInPTA Collaboration, Antoniadis, J., et al. 2023, A&A, 678, A50
Ferrarese, L., & Merritt, D. 2000, ApJL, 539, L9
Gardiner, E. C., Kelley, L. Z., Lemke, A.-M., & Mitridate, A. 2024, ApJ, 965, 164
Gebhardt, K., Bender, R., Bower, G., et al. 2000, ApJL, 539, L13
Geris, S., Maiolino, R., Isobe, Y., et al. 2026, MNRAS, 545, staf1979
Greene, J. E., Seth, A., Kim, M., et al. 2016, ApJL, 826, L32
Greene, J. E., Strader, J., & Ho, L. C. 2020, ARA&A, 58, 257
Guia, C. A., & Pacucci, F. 2024, RNAAS, 8, 153
Gültekin, K., Richstone, D. O., Gebhardt, K., et al. 2009, ApJ, 698, 198
Gültekin, K., Tremaine, S., Loeb, A., & Richstone, D. O. 2011, ApJ, 738, 17
Harikane, Y., Zhang, Y., Nakajima, K., et al. 2023, ApJ, 959, 39
Harris, C. J., Gültekin, K., & Blecha, L. 2026, arXiv:2601.07762
Hirschmann, M., Khochfar, S., Burkert, A., et al. 2010, MNRAS, 407, 1016
Hu, H., Inayoshi, K., Haiman, Z., Ho, L. C., & Ohsuga, K. 2025, ApJL, 983, L37
Huber, M. C., Simon, J., & Comerford, J. M. 2025, ApJ, 988, 90
Izquierdo-Villalba, D. 2026, A&A, 708, A303
Jahnke, K., & Macciò, A. V. 2011, ApJ, 734, 92
Jones, B. L., Kocevski, D. D., Pacucci, F., et al. 2025, arXiv:2510.07376
Kelley, L. Z., Blecha, L., & Hernquist, L. 2017, MNRAS, 464, 3131
Kelley, L. Z., Gardiner, E. C., Wright, D., et al. 2024, nanograv/holodeck: v1.5.2, Zenodo, doi:10.5281/zenodo.10966412
Kocsis, B., & Sesana, A. 2011, MNRAS, 411, 1467
Kormendy, J., & Gebhardt, K. 2001, AIPC, 586, 363
Kormendy, J., & Ho, L. C. 2013, ARA&A, 51, 511
Laal, N., Taylor, S. R., Matt, C., & Gultekin, K. 2026, ApJ, 1004, 90
Lauer, T. R., Tremaine, S., Richstone, D., & Faber, S. M. 2007, ApJ, 670, 249
Leja, J., Speagle, J. S., Johnson, B. D., et al. 2020, ApJ, 893, 111
Li, J., Shen, Y., & Zhuang, M.-Y. 2025a, arXiv:2502.05048
Li, J., Silverman, J. D., Shen, Y., et al. 2025b, ApJ, 981, 19
Liepold, E. R., & Ma, C.-P. 2024, ApJL, 971, L29
Maiolino, R., Scholtz, J., Witstok, J., et al. 2024, Natur, 627, 59
Matt, C., Gültekin, K., Kelley, L. Z., et al. 2026, ApJ, 997, 188
Matt, C., Gültekin, K., & Simon, J. 2023, MNRAS, 524, 4403
McConnell, N. J., & Ma, C.-P. 2013, ApJ, 764, 184
Mountrichas, G. 2023, A&A, 672, A98
Pacucci, F., Nguyen, B., Carniani, S., Maiolino, R., & Fan, X. 2023, ApJL, 957, L3
Peng, C. Y. 2007, ApJ, 671, 1098
Phinney, E. S. 2001, arXiv:astro-ph/0108028
Planck Collaboration, Ade, P. A. R., Aghanim, N., et al. 2014, A&A, 571, A16
Reardon, D. J., Zic, A., Shannon, R. M., et al. 2023, ApJL, 951, L6
Reines, A. E., & Volonteri, M. 2015, ApJ, 813, 82
Rodriguez-Gomez, V., Genel, S., Vogelsberger, M., et al. 2015, MNRAS, 449, 49
Sato-Polito, G., Zaldarriaga, M., & Quataert, E. 2024, PhRvD, 110, 063020
Schulze, A., & Wisotzki, L. 2014, MNRAS, 438, 3422
Sesana, A. 2013, CQGra, 30, 224014
Shankar, F., Bernardi, M., Richardson, K., et al. 2019, MNRAS, 485, 1278
Shankar, F., Bernardi, M., Sheth, R. K., et al. 2016, MNRAS, 460, 3119
Silverman, J. D., Li, J., Ding, X., et al. 2025, ApJL, 995, L67
Simon, J. 2023, ApJL, 949, L24
Simon, J., & Burke-Spolaor, S. 2016, ApJ, 826, 11
Stone, M. A., Lyu, J., Rieke, G. H., Alberts, S., & Hainline, K. N. 2024, ApJ, 964, 90
Sun, Y., Lyu, J., Rieke, G. H., et al. 2025a, ApJ, 978, 98
Sun, Y., Rieke, G. H., Lyu, J., et al. 2025b, ApJ, 983, 165
Terrazas, B. A., Aird, J., & Coil, A. L. 2025, ApJ, 993, 187
Tremaine, S., Gebhardt, K., Bender, R., et al. 2002, ApJ, 574, 740
Übler, H., Maiolino, R., Curtis-Lake, E., et al. 2023, A&A, 677, A145
Vestergaard, M., & Peterson, B. M. 2006, ApJ, 641, 689
Volonteri, M. 2012, Sci, 337, 544
Volonteri, M., Habouzit, M., & Colpi, M. 2023, MNRAS, 521, 241
Wyithe, J. S. B., & Loeb, A. 2003, ApJ, 595, 614
Xu, H., Chen, S., Guo, Y., et al. 2023, RAA, 23, 075024
Yue, M., Eilers, A.-C., Simcoe, R. A., et al. 2024, ApJ, 966, 176
Zhang, H., Behroozi, P., Volonteri, M., et al. 2023, MNRAS, 523, L69
Zhang, Y., Ouchi, M., Gebhardt, K., et al. 2023, ApJ, 948, 103
Zhu, B., & Springel, V. 2025, MNRAS, 543, 2489
Zhuang, M.-Y., & Ho, L. C. 2023, NatAs, 7, 1376
Ziparo, F., Carniani, S., Gallerani, S., & Trefoloni, B. 2026, arXiv:2603.04358
Zou, F., Brandt, W. N., Gallo, E., et al. 2024, ApJ, 976, 6